DEVELOPMENT OF REDUCED-ORDER MESHLESS SOLUTIONS OF THREE-DIMENSIONAL NAVIER STOKES TRANSPORT PHENOMENA

A Thesis

Presented in Partial Fulfillment of the Requirements for

the Bachelor of Science of Civil Engineering in

the College of Engineering of The Ohio State University

By

Daniel Benjamin Work

* * * * *

The Ohio State University
2006

Examination Committee:

Approved By

Dr. Oliver G. McGee, III, Adviser

Dr. Patrick J. Fox

Adviser
Department of Civil Engineering

Dedicated to Mom and Dad

ABSTRACT

Emerging meshless technologies are very promising for numerically solving Euler and Navier-Stokes transport systems in one-, two-, and three-dimensions (3-D). The Reduced-Order Meshless (ROM) technique developed in this work is applicable to a wide array of transport physics systems (i.e., fluid flow, heat transfer, gas dynamics, internal combustion flow and chemical reactions, and solid-liquid mixture flow) with various types of boundary and initial conditions. Such applications to be benchmarked in this work include one- and two-dimensional advection, and two- and three-dimensional convection-diffusion problems (Burgers' equation). Computational solutions to these boundary-value problems will be demonstrated using the ROM approach and the predicted solutions will be posted against the Meshless Local Petrov-Galerkin (MLPG) method and exact solutions to these problems when they exist. Extensions to 3-D phenomenology will be attempted based on the conclusions obtained from computational studies to establish the existence, smoothness, and boundedness of 3-D Navier-Stokes transport systems.

An approximated benchmark solution of the Navier-Stokes equations is also developed in this work using a linearized perturbation analysis. The classical paper on gas turbine throughflow, *Three Dimensional Flows in Turbomachines* (Marble, 1964), outlines this procedure for approximation, and produces solutions for a class of axisymmetric problems. An investigation into the behavior of these solutions uncovered

a series of inconsistencies in the paper, which are outlined in detail and corrected when known to be in error.

FIELDS OF STUDY

Major Field: Civil Engineering

AKNOWLEDGEMENTS

I sincerely thank my advisor, Dr. Oliver G. McGee for teaching the process of research and discovery, for introducing me to *absentee teachers*, and for inspiring me to achieve my goals. You are a great friend and mentor.

I am indebted to Dr. Chih Fang for his generous intellectual and technical support throughout this project.

I thank Keith Coleman and Celeste Chavis for making the Summer of 2005 extremely rewarding *and* entertaining.

This research was supported by The Ohio State University College of Engineering.

TABLE OF CONTENTS

TABLE OF FIGURES

1. INTRODCUTION

Transport physics problems are practical and full of complexities that remain hard to fully understand. The current state of our knowledge presents several conflicting conjectures about the existence, uniqueness, and smoothness of solutions of one such problem, the Navier-Stokes equations. Because our current knowledge leaves open the question of whether these solutions even exist, our understanding of these systems is at a very primitive level. Conventional methods of partial differential equations appear to be inadequate to settle the question. However, innovative approaches in advancing computational meshless techniques may be able to settle the inquiry, and lead to advances in fluids engineering and science. This is the primary goal that is revealed through the development and application of meshless technologies to advection-diffusion and convection-diffusion problems, Burgers' equation, and axisymmetric Navier-Stokes transport systems.

A Reduced-Order Meshless (ROM) methodology has been developed that can capture the three-dimensional transport physics of flow devices more accurately and efficiently than current state-of-the-art meshless technologies. Specifically, the system is modeled as a meshless continuum utilizing only nodal data to describe the arbitrary volume in which the system's governing equations are solved, subjected to constraints imposed by an assumed transport field of mathematically complete, generalized Fourier series of functions. The Fourier series comprises a basis for the transport physics domain containing the desired solution (i.e., pressure, temperature, density, velocities, enthalpy, and entropy at a particle inside the transport system). No conventional finite elements,

boundary element, finite difference, finite volume, and element connectivity or component substructuring of data is needed.

In this work, computational solutions to the aforementioned boundary-value problems are demonstrated using the ROM approach and are posted against exact solutions to these problems when they exist. At this stage in the research, exact solutions to one- and two-dimensional advection-diffusion and convection-diffusion, and three dimensional Burger's equations have been calculated. These equations are commonly used as test equations for the Navier-Stokes equations because closed-form solutions exist for the two-dimensional problem. A classical linearized perturbation analysis of the Navier-Stokes equations is developed as a benchmark for fully three-dimensional asymmetric through-flow nonlinear problems of turbomachines in progress. In comparison to other reduced-order meshless models, our results are a significant advancement in the ability to capture linear advection and nonlinear convection effects of these equations.

The Navier Stokes Equations

The search to solve Euler and Navier-Stokes transport systems in one-, two-, and three-dimensions, has been aided with significant advances in emerging meshless computational tools. These equations are to be solved for an unknown transport property (ϕ), which can be either a scalar or vector quantity (i.e., density, temperature, energy, entropy (losses), or a fluid velocity vector $u_i(x,t)_{i=1,2,3}$), passing across a velocity field $u_j(x,t)_{j=1,2,3}$, and fluid pressure $p(x,t)$ defined in a transport domain at position x and time t

> 0. This work will restrict attention to incompressible transport problems. The 3-D Navier-Stokes equations are then given by:

$$\frac{\partial}{\partial t} f_i + \sum_{j=1}^{n} u_j \frac{\partial f_i}{\partial x_j} = n\Delta f_i - \frac{\partial p}{\partial x_i} + f_i(x,t) \qquad (1.1)$$

$$div\ u = \sum_{j=1}^{n} \frac{\partial f_i}{\partial x_j} = 0 \qquad (1.2)$$

with initial conditions $\phi(x,0) = \phi^o(x)$ = the prescribed transport property values. Here, $f_i(x,t)$ are the components of a given, externally applied source in the transport system, ν represents a transport diffusion constant associated with ϕ, and $\Delta = \sum_{i=1}^{3} \frac{\partial^2}{\partial x_i^2}$ is the Laplacian operator in the space variables. The Euler equations are (1) and (1.2) with the transport diffusion ν set to zero. Equation (1.1) is defined as the conservation of momentum for a transport system subject to externally applied sources, internal pressure $p(x,t)$, and transport diffusion effects. Equation (1.2) defines the transport system as incompressible, assumption this work will be restricted to.

A few words defining each of the terms in Equation (1.1) is appropriate. The first term on the left-hand side (LHS) of Equation (1.1) is *unsteadiness* of the property ϕ. The second LHS term of Equation (1.1) is the *nonlinear convection* term. It is nonlinear because it can involve products of the unknown transport property (ϕ), its gradients, and the velocity field $u_j(x,t)_{j=1,2,3}$. The first term on the right-hand side (RHS) of Equation (1.1) is the *diffusion* term, involving the Laplacian operator in the spatial domain of the transport system. This diffusion term represents the friction or shearing applied on the transport system. The second RHS term of Equation (1.1) is the transport pressure

gradient term. It represents the internal normal stress rates that exist in the transport system. The last RHS term of Equation (1.1) is the externally applied source term in the transport system, resulting from either gravitational/centrifugal body forces or surface traction forces existing at the boundary surfaces of the transport system.

The existence of the nonlinear convection term resulting from a substantial derivative in time and space of the dependent transport property (ϕ), poses the central difficulty in obtaining tractable solutions of Equation (1.1), both mathematically exact or computationally. As the convection term dominates, computational solutions become notoriously unstable, exhibiting oscillatory solutions about an unknown exact solution. Conventional treatment is to stabilize numerical approximations (such as Finite Difference Methods (FDM), Finite Element Methods (FEM), Finite Volume Methods (FVM), and Boundary Element Methods (BEM)) using numerically-correcting upwinding techniques. Emerging meshless technologies (Atluri, 2002; Liu, 2003) have also considered similar kinds of special treatments, which limit the ability to predict the existence and smoothness of unsteady convection-diffusion transport systems characterized by the Navier-Stokes equations. Hence, the primary focus of this research is to address this specific question:

Can new emerging meshless technologies in reduced-order simulation and modeling be used to find computationally exact solutions to 3-D Navier-Stokes transport systems, where conventional integral-based finite element and differential-based finite volume methodologies under serve the analysis of such systems?

Methods of Procedure

Advanced engineering computations have seen a great deal of progress during the past four decades. The conventional methodologies have employed Lagrangian-based (integral) FEM and BEM, and Eulerian-based (differential) FDM and FVM. Lagrangian-based FEMs and BEMs have several drawbacks in modeling and simulation of the above Euler and Navier-Stokes fluid systems. These drawbacks result from either the BEMs' inherent difficulties in preventing the integral-based singular functions from producing solution matrix ill-conditioning, or the FEMs' false numerical "locking" in convection, diffusion, compressibility, and unsteadiness phenomena. Both FEMs and BEMs are further disadvantaged by the need to (re)generate meshes at an enormous computational cost. Eulerian-based FDMs and FVMs have setbacks of "ghost" point evaluations along the wall boundaries of fluid systems. Moreover, when simulating the loss mechanisms of fluid flow problems, FDMs and FVMs can suffer special computational anomalies in systems with large distortions, moving material or density interfaces, and deformable boundaries or walls. Previous attempts have been made to combine the best of FDMs, FVMs, and FEMs, by combining the multi-grid systems with an Arbitrary Lagrangian-Eulerian (ALE) coupling approach (Shin and Chisum, 1997). However, such approaches have very complicated mapping techniques which can lead to problems of stability and accuracy.

Due to the time consuming mesh generation and computational cost of regenerating the meshes, a new field of meshless methods have been developed to overcome this burden. However, the majority of these methods (as outlined in Lin, 2000), namely Smooth Particle Hydrodynamics (SPH) (Lucy, 1977), Diffuse Element

Method (DEM) (Naroles *et al*, 1992), Element Free Galerkin Method (EFG) (Belytcsko *et al*, 1994), Reproducing Kernel Particle Method (RKPM) (Liu, Jun, and Zhang, 1995), and hp-clouds method (Duarte and Oden, 1996), are not truly mesh free. These methods require a mesh to interpolate or to numerically integrate the weak form of the governing equation.

Four truly meshless methods have been developed, including the Finite Point Method (FPM) (Oñate, Idelsohn, Zeinkiewicz and Talyor, 1996), Local Boundary Integral Equation Method (LBIE) (Zhu, Zhang, and Atluri, 1998a,b), Meshless Local Petrov Galerkin Method (Lin and Atluri, 2000), and the Reduced-Order Meshless (ROM) (McGee and Fang, 2005). The scope of this work is limited to the latter two methods.

The MLPG method is a *weak (integral) form* of the solution computed over a local simple geometry sub-domain. The governing equation is weighted by a test function and integrated over the local domain to form a global stiffness matrix. A moving least squares method is used to determine the value of the coefficients for the solution. The specific shape of the domain (cube, sphere, etc) can be modified to suit the global boundary conditions, yielding applicability to a wide range of boundary-value problems. The major drawback from this method is its tendency to exhibit oscillatory solutions for convection driven problems. Specifically, as the inertial (convective) forces become large, the solution is pushed in the direction of the flow, and the diffusion process is dominated. Upwinding techniques, originally developed to stabilize highly oscillatory first and higher order derivatives inside FEM and FVM methods, can also be implemented to MLPG to emphasize upstream conditions for the solution of each point. The major difficulty in developing an upwinding scheme for nonlinear convection

problems is that the flow direction is not known until after the solution is developed. Models implementing upwinding lose transportiveness, being the ability for flow properties to be transported in all directions of the domain.

The first upwinding technique (MLPG1) developed in Atluri (2002) is implemented through the choice of the trial function. The maximum value of the weighting function can be shifted up in the direction of the streamline function, while the domain of the function remains constant. A second correction scheme (MLPG2) is developed which uses an upstream shift of the entire domain of the unskewed trail function. Both methods are benchmarked in this work.

The ROM technique is unique in that it is a *strong form* solution. The partial differential equation is solved directly without the use of numerical integration by invoking an assumed generalized Fourier series, which is a unique, continuous solution throughout the entire domain of interest. Boundary and initial conditions are included in the approximating series. Lower order derivatives of the given field may be calculated exactly and substituted into the governing equation at each arbitrary node in the domain. The partial differential equation over the entire domain is effectively transformed into a series of algebraic equations evaluated at each node, to be solved for unknown coefficients using standard methods for evaluating systems of equations. No element connectivity is required, albeit the solution is dependent on the choice of the evaluation points.

2. NUMERICAL ANALYSIS

To determine the effectiveness of the ROM methodology, a series of examples are in this work.

1D Advection-Diffusion Boundary-Value Problem

Consider the simple one-dimensional advection-diffusion equation described as:

$$u\frac{\partial f}{\partial x} - K\frac{\partial^2 f}{\partial x^2} - f = 0 \qquad (2.1)$$

where the three terms from left to right are the advection, diffusion, and source terms respectively. The constant K is the diffusion coefficient, and u is the coefficient associated with advection. The relative size of the advection and diffusion terms are determined by the non-dimensional Peclet (Pe) number defined as $Pe = \frac{uL}{K}$, with L as the characteristic length scale. Equation (2.1) is subject to the following boundary conditions:

$$f(0) = 0, \quad f(1) = 0\,. \qquad (2.2)$$

For low order Peclet numbers, there is excellent agreement between the ROM, MLPG, and the exact solution (Figure 2.1). At Pe=100, the MLPG method begins to exhibit oscillatory behavior due to the large advection term. The upstream direction in the one-dimensional problem is trivial, and both upwinding techniques adequately predict the exact solution. When the Peclet number is increased again to 1000, the MLPG method completely diverges out of the figure. Although the MLPG2 appears to capture the exact solution, the plot is misleading. With the exact solution plotted to only 10 points, the sharp boundary effect is masked. The MLPG1 and MLPG2 techniques do not

accurately predict the solution in the domain between x=0.9 and x=1. In this problem, the ROM technique predicts the solution at high Peclet numbers without the need for any upwinding. In addition, the effect of the boundary at x=1 is captured better than either of the MLPG methods.

ROM **Lin *et al* (2000) MLPG**

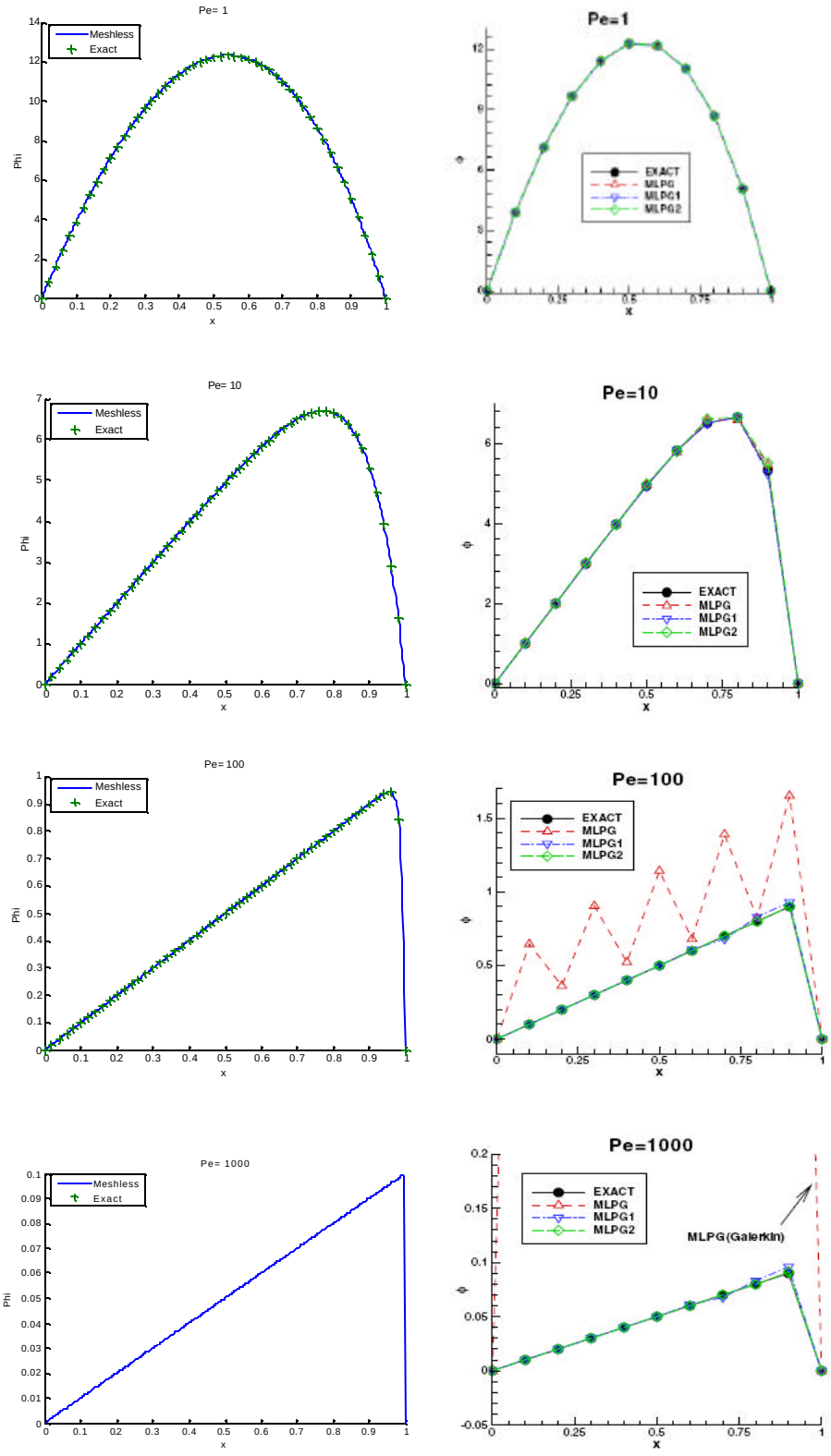

Figure 2.1

2D Advection-Diffusion Boundary-Value Problems

Consider now the two-dimensional advection diffusion equation written as:

$$u\frac{\partial f}{\partial x}+v\frac{\partial f}{\partial y}-K\frac{\partial^2 f}{\partial x^2}-K\frac{\partial^2 f}{\partial y^2}-f=0 \tag{2.3}$$

The boundary conditions are given by:

$$\begin{aligned} &f(x,1)=f(1,y)=0\\ &f(x,0)=1-x\\ &f(0,y)=1-y \end{aligned} \tag{2.4}$$

The source *f=0,* and the direction of the flow is skewed 45 degrees from the x axis using the advection coefficients given by:

$$u=\cos(p/4),\ v=\sin(p/4) \tag{2.5}$$

For this and subsequent examples, only the best upwinding scheme (MLPG2) will be compared with the upwind free ROM results. Figure 2.2 shows both methods in good agreement for low Peclet number systems. However, as the advection term dominates, the ROM method is able to accurately capture the flow around the x=1 and y=1 boundaries. The MLPG2 scheme has difficulty predicting the nature of the solution in the neighborhood of (x,y)=(1,1), and is unable to capture the boundary layer. At a Peclet number of 100, ROM predicts a steep transport gradient associated with the boundary layer effect. At $Pe=10^6$, the boundary layer creates a nearly vertical gradient which is not captured in the MLPG2 method. In fact, the MLPG2 method does not capture any noticeable change in solution from Pe=100 to $Pe=10^6$ along the boundary. The coarseness of the grid creates false diffusion in the solution space near the boundary, which is especially obvious in the neighborhood of (x,y)=(1,1). In general, the MLPG method does not capture the steep gradients produced near the boundary in either the one-

or two-dimensional problems. It is projected the *weak* formulation of the partial differential equation in the MLPG method may necessitate a course grid to prevent matrix ill conditioning.

ROM **Lin *et al* (2000) MLPG2**

Pe=10

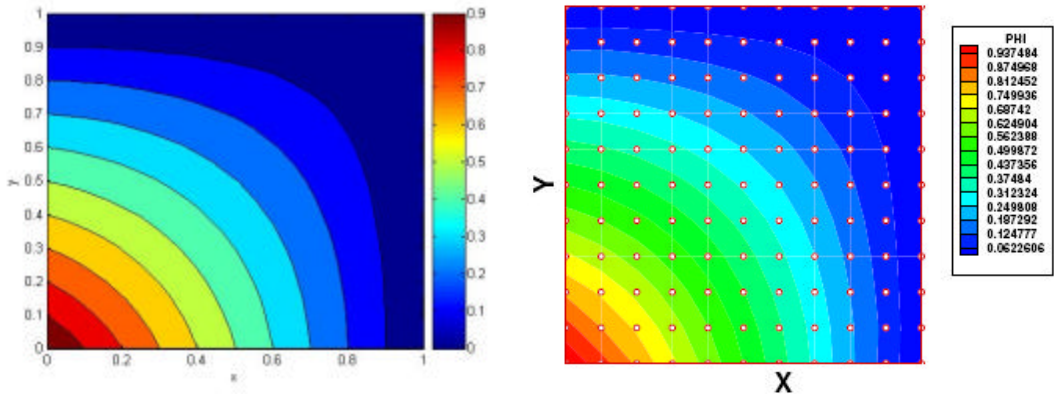

Pe=100

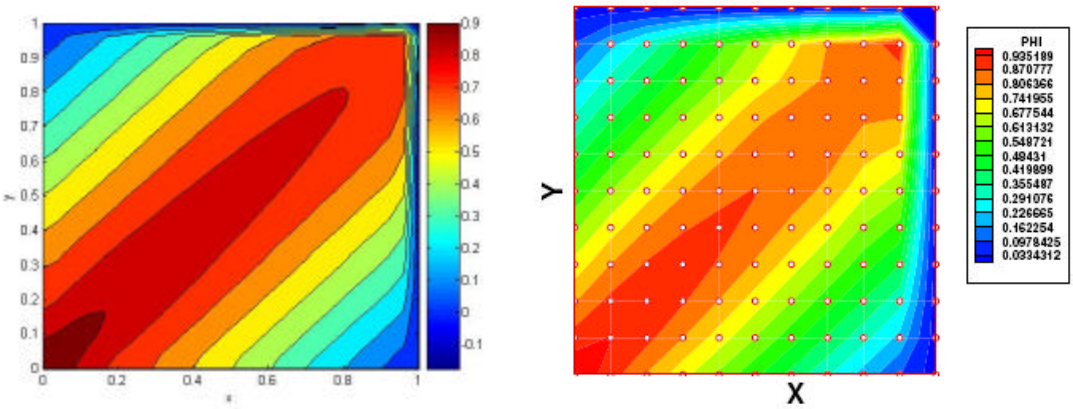

Pe=10e6

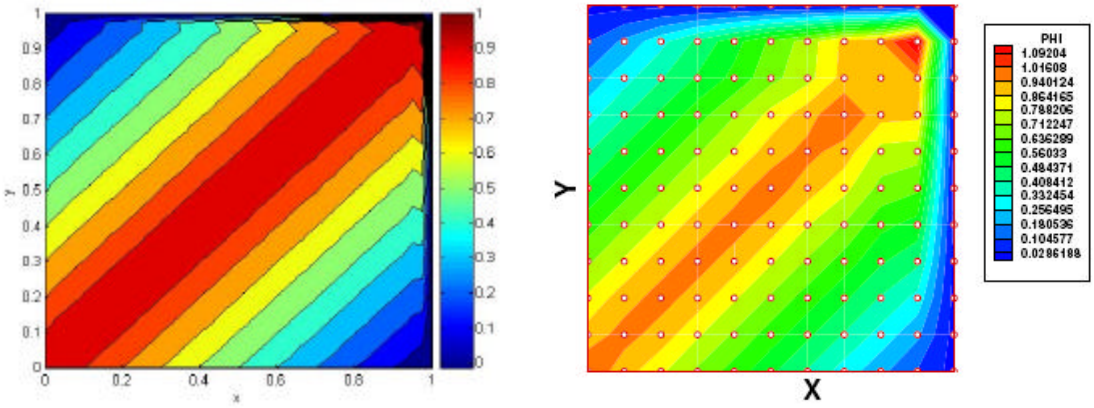

Figure 2.2

A second two-dimensional example is examined using the governing equation (2.3), subject to the condition $f = 0$ on all boundaries. The advection coefficients u and v are given as one and zero respectively, which eliminates the advection term in the y-direction. However, the diffusion process and the boundary conditions at x=1 and x=0 make the problem a two dimensional process. In addition, the equation is subject to an external forcing function is given by:

$$f = \begin{cases} 1, & (0 < x \le 0.5) \\ -1, & (0.5 < x < 1) \end{cases} \tag{2.6}$$

ROM **Lin *et al* (2000) MLPG2**

Pe =10^6

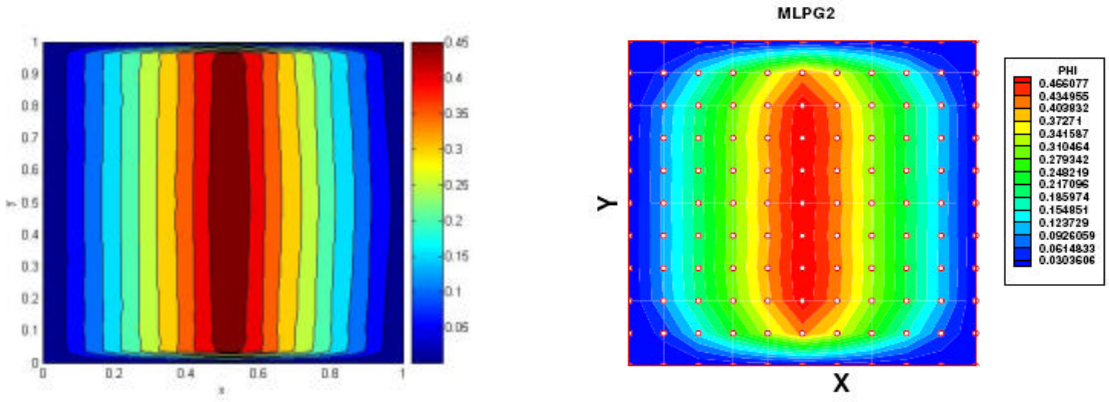

Figure 2.3

The wall boundary conditions at y=1 and y=0 creates a thin boundary layer flow called the "wall effect", which is accurately picked up by the ROM solution. Similar to the previous two-dimensional example, the ROM methodology captures the steep solution gradient near the boundary including the "mixing phenomena" with the main

flow above the boundary layer. Both the boundary layer flow and the adjacent mixing phenomena are highly irreversible (entropic) phenomenon having large amounts of shear stresses picked up by the diffusion terms of the advection-diffusion equation. Mixing taking place adjacent to the boundary layer flow is a shear driven process of high irreversibility. The best MLPG upwinding scheme captures the appropriate solution in a horizontal band near the center of the y solution space. However, as the vertical position nears a boundary, MLPG2 underestimates the entropic effect and it does not predict any mixing phenomena in the solution.

2D Convection-Diffusion Boundary-Value Problem

Up to this point, the convection term of the Navier Stokes equation has been approximated by a known advection term. While a large advection term creates essentially the same inertial force dominated flow, the simplification allows the solution to be solved using the ROM technique without any iteration. The principle point of the preceding numerical examples was to verify the ROM methodology's capability to handle the boundary effects, which plague not only conventional finite element, finite difference, and finite volume schemes, but also mesh and mesh-free convection-diffusion schemes even with the use of upwinding. This work is restricted to these non-iterative problem formulations, but the ROM technique has been demonstrated on highly nonlinear solid mechanics applications by McGee *et al* (2005a,b) and Fang *et al* (2005). This current work has been expanded by the same authors to the two-dimensional Burger's equations, given by:

$$u\frac{\partial u}{\partial x}+v\frac{\partial u}{\partial y}-\frac{1}{\mathrm{Re}}\left(\frac{\partial^2 u}{\partial x^2}+\frac{\partial^2 u}{\partial y^2}\right)=0 \qquad (2.7)$$

$$u\frac{\partial v}{\partial x}+v\frac{\partial v}{\partial y}-\frac{1}{\mathrm{Re}}\left(\frac{\partial^2 v}{\partial x^2}+\frac{\partial^2 v}{\partial y^2}\right)=0 \tag{2.8}$$

Subject to the boundary conditions given as:

$$u(0)=v(0)=0,\ u(L)=2\tanh\left(\frac{p}{3}\mathrm{Re}\right),\ v(L)=\frac{2}{\mathrm{Re}}\tan\left(\frac{p}{3}\right) \tag{2.9}$$

These equations are commonly used as test models for Navier-Stokes solvers, because they contain the same nonlinear convection term, and the two-dimensional form has exact solutions. The low Reynolds number (ratio of nonlinear convection to diffusion) solutions are compared against the exact solution in Figure 2.4, and are in good agreement.

Exact Solution

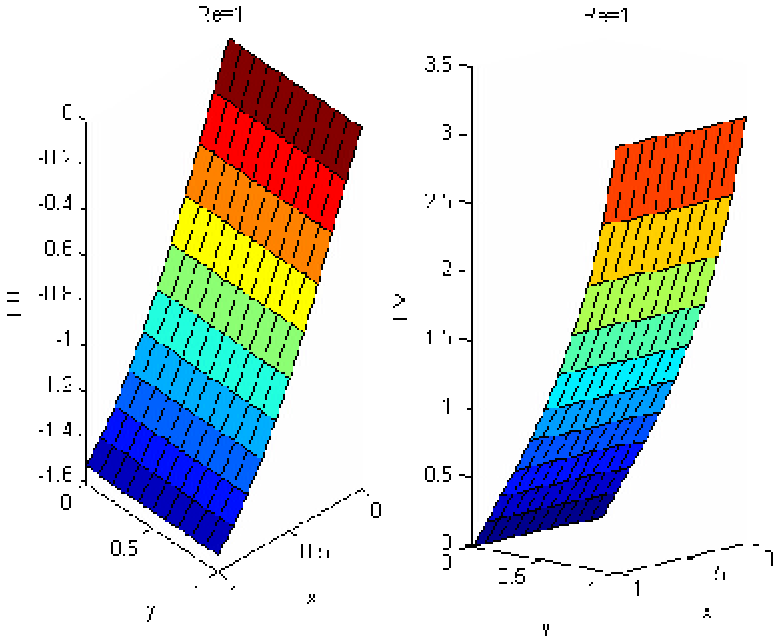

ROM Solution

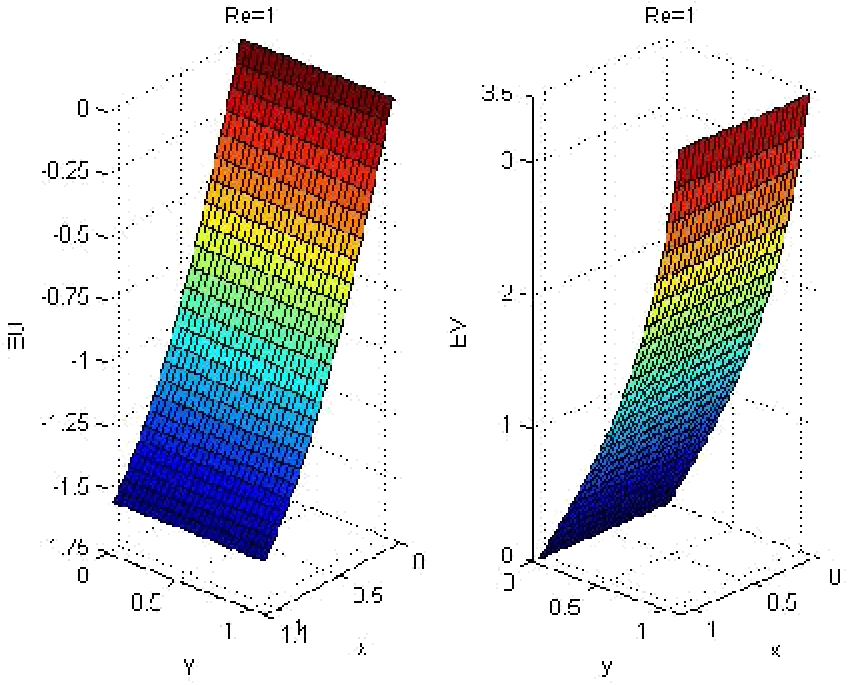

Figure 2.4

3D Convection-Diffusion Boundary-Value Problem

The three-dimensional Burger's equations are given by:

$$u\frac{\partial u}{\partial x}+v\frac{\partial u}{\partial y}+w\frac{\partial u}{\partial z}-\frac{1}{\mathrm{Re}}\left(\frac{\partial^2 u}{\partial x^2}+\frac{\partial^2 u}{\partial y^2}+\frac{\partial^2 u}{\partial z^2}\right)=1 \tag{2.10}$$

$$u\frac{\partial v}{\partial x}+v\frac{\partial v}{\partial y}+w\frac{\partial v}{\partial z}-\frac{1}{\mathrm{Re}}\left(\frac{\partial^2 v}{\partial x^2}+\frac{\partial^2 v}{\partial y^2}+\frac{\partial^2 v}{\partial z^2}\right)=1 \tag{2.11}$$

$$u\frac{\partial w}{\partial x}+v\frac{\partial w}{\partial y}+w\frac{\partial w}{\partial z}-\frac{1}{\mathrm{Re}}\left(\frac{\partial^2 w}{\partial x^2}+\frac{\partial^2 w}{\partial y^2}+\frac{\partial^2 w}{\partial z^2}\right)=1 \tag{2.12}$$

with boundary conditions given by:

$$u(0)=v(0)=w(0)=0,\ u(L)=v(L)=w(L)=0 \tag{2.13}$$

The resulting solution (Figure 2.5) for Re = 1 again demonstrates the ROM ability to capture solutions to nonlinear problems, when the convection term is on the same order of magnitude as the diffusion term. One of the goals of future work is to expand these solutions to higher-order Reynolds number flows, where the convection term substantially drives the solution.

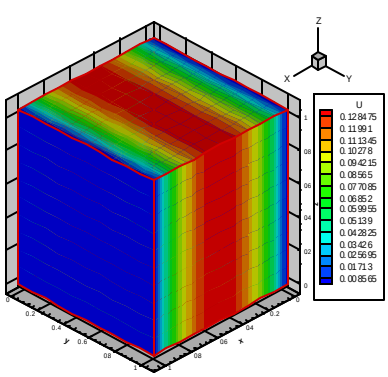

u(x,y,z)

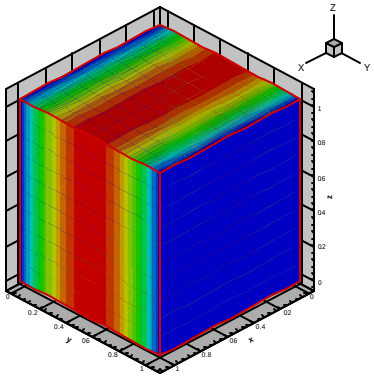

v(x,y,z)

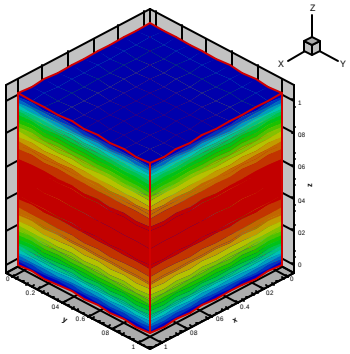

w(x,y,z)

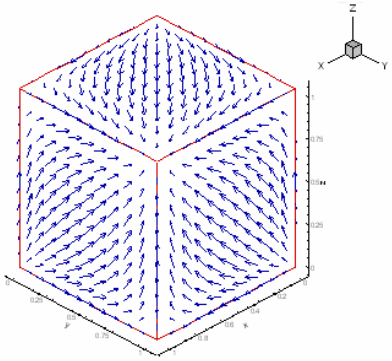

Resultant Fluid Velocities

Figure 2.5

3. NAVIER STOKES APPROXIMATION- A THROUGHFLOW ANALYSIS

In addition to developing solutions to large *Re* Burger's equation, an approximate solution for the Navier-Stokes equations in three dimensions must be developed, because no exact solution exists for general cases of three dimensional Burger's or Navier-Stokes equations. The primary purpose of the approximate solution is to produce some confidence in the solutions that will be developed using ROM. While the literature is filled with numerical solutions, relatively few closed-form solutions exist. One such method was developed by Frank Marble (1964) for developing an analysis of the throughflow of a gas turbine engine. The behavior of the machine is governed by examining three types of aerodynamic flow problems: (1) throughflow - the amount of air that can pass through the machine with a given geometry, (2) blade-to-blade - the air flow velocity triangles defining the pressurized flow characteristics between blade rows of the engine, and (3) three-dimensional secondary flow - a detailed analysis of the loss mechanisms associated with blade tip clearance flow, the endwall flow and the associated boundary layer effects. This work focuses on the first problem, where the blade rows can be reduced to momentum sources in the axial, radial and tangential directions. By making this initial assumption, a general velocity profile of the machine can be determined, which will then become input parameters for solving the more detailed blade-to-blade interactions and loss mechanisms (problems 2 and 3) of the machine. Marble's work advanced the state of aircraft engine design by considering the axisymmetric Navier-Stokes equations through linearized incompressible and inviscid solutions.

Development of linearized solutions

The axisymmetric, steady Navier-Stokes equations in cylindrical coordinates (r,θ,z) are given by:

$$u\frac{\partial u}{\partial r}+w\frac{\partial u}{\partial z}-\frac{v^2}{r}=-\frac{1}{r}\frac{\partial p}{\partial r}+F_r \tag{3.1}$$

$$u\frac{\partial (rv)}{\partial r}+w\frac{\partial (rv)}{\partial z}=rF_q \tag{3.2}$$

$$u\frac{\partial w}{\partial r}+w\frac{\partial w}{\partial z}=-\frac{1}{r}\frac{\partial p}{\partial z}+F_z \tag{3.3}$$

$$\frac{1}{r}\frac{\partial (rru)}{\partial r}+\frac{\partial (rw)}{\partial z}=0 \tag{3.4}$$

where equations 3.1, 3.2, & 3.3 are the radial, axial and tangential momentum equations, subject to the continuity equation (3.4). The velocity profiles are given by (u,v,w) in the (r,θ,z) directions, and r and p are the density and pressure respectively. Due to the axial symmetry assumption, all derivatives with respect to θ vanish. The inviscid assumption further simplifies the equations by eliminating the diffusion process which is very small for high Reynolds number air flows.

These equations are nonlinear because of the convection term in the three momentum equations. Also adding to the nonlinearity are the force terms from the blade rows, which are functions of the velocity profile in the region of the blade. Finally, the density adds another source of nonlinearity to the equations. However, the equations can be approximated using a linearized perturbation analysis, if a simple geometry for the gas turbine engine is used (Marble, 1964; Figure 3.1).

Problem Geometry, Marble (1964)

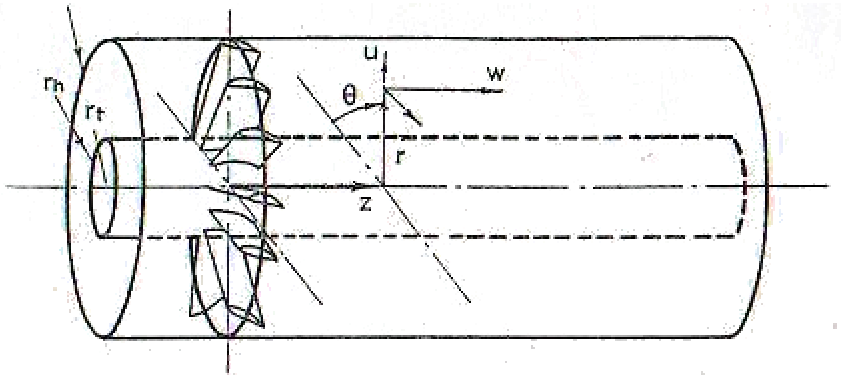

Figure 3.1

By assuming a constant hub radius (r_h) and a constant tip radius (r_t), the basic shape of the streamlines are known in advance of the solution. Furthermore, the overall increase in momentum due to the externally applied source (blade rows) is relatively small compared to the base momentum in the system. Lastly, compressibility effects can be ignored for low speed (Mach<<1) flows.

Given these restrictions, Marble outlines a useful perturbation analysis where the unknown transport properties f = u,v,w, etc. are approximated by:

$$f = f^{(0)} + e f^{(1)} + \ldots \tag{3.5}$$

and high-order terms are dropped. The $f^{(0)}$ terms are just the initial conditions of the system. This process transforms the governing equations 3.1-3.4 into a linear second-order partial differential equation (PDE), which takes the form of a non-homogeneous Bessel's equation with a harmonic term in the z direction given as:

$$\frac{\partial^2 u^{(1)}}{\partial r^2} + \frac{1}{r}\frac{\partial u^{(1)}}{\partial r} - \frac{1}{r^2}u^{(1)} + \frac{\partial^2 u^{(1)}}{\partial z^2} = -\frac{1}{w^{(0)}}\frac{\partial F_z}{\partial r} = -\frac{1}{w^{(0)}}\frac{\partial}{\partial z}\left(\frac{\partial h^{(1)}}{\partial r}\right) \tag{3.6}$$

Equation 3.6 is only a function of the radial velocity perturbation and a prescribed axial force (F_z), which is given as a prescribed enthalpy ($h^{(1)}$) jump across the blade row. This equation can be solved independently of the axial perturbation, which is then calculated through the continuity equation:

$$\frac{\partial w^{(1)}}{\partial z} = -\frac{1}{r}\frac{\partial (r u^{(1)})}{\partial r} \tag{3.7}$$

Constant Hub Constant Tip Actuator Disk Problem

The simplest solution to equation 3.6 can be developed by assuming the enthalpy jump occurs across a blade row with infinitesimal length at z=0 given by:

$$h^{(1)}(r) = a w^{(0)} w r_t \left(\frac{r}{r_t} \right)^2 \tag{3.8}$$

The solution is subject to the following boundary conditions:

$$u^{(1)}(r_h, z) = u^{(1)}(r_t, z) = 0 \tag{3.9}$$

$$u^{(1)}(r, -\infty) = u^{(1)}(r, \infty) = 0 \tag{3.10}$$

which ensures the radial perturbation vanishes far upstream and downstream from the blade row (3.9) and the velocity normal to the surface of the hub and tip is zero (3.10). Additional matching conditions must be prescribed over the singular enthalpy jump source at z=0 and are given as:

$$u^{(1)}(r, 0^+) = u^{(1)}(r, 0-) \tag{3.11}$$

$$\left[\frac{\partial u^{(1)}}{\partial z} \right]_{0-}^{0+} = -\frac{1}{w^{(0)}} \left[\frac{\partial h^{(1)}}{\partial r} \right]_{0-}^{0+} \tag{3.12}$$

Given the boundary conditions, radial and axial perturbation complementary solutions to the coupled equations 3.6 and 3.7 can be given in terms of Bessel functions of the first kind ($J_1(x)$) and second kind ($Y_1(x)$) as:

$$u^{(1)} = \sum_1^\infty C_n \left[J_1(k_n r) Y_1(k_n r_h) - J_1(k_n r_h) Y_1(k_n r) \right] e^{-k_n |z|} \tag{3.13}$$

$$w^{(1)} = -\sum_1^\infty C_n \left[J_0(k_n r) Y_1(k_n r_h) - J_1(k_n r_h) Y_0(k_n r) \right] e^{-k_n |z|} \quad z < 0 \tag{3.14}$$

$$\begin{aligned} w^{(1)} = & \sum_1^\infty C_n \left[J_0(k_n r) Y_1(k_n r_h) - J_1(k_n r_h) Y_0(k_n r) \right] e^{-k_n |z|} \\ & - 2 \sum_1^\infty C_n \left[J_0(k_n r) Y_1(k_n r_h) - J_1(k_n r_h) Y_0(k_n r) \right] \quad z \geq 0 \end{aligned} \tag{3.15}$$

An interesting result of the continuity equation yields the axial perturbation at z=0 is just half of the residual axial velocity far downstream. In general, this result will hold true for any problem geometry and source which produces symmetric radial perturbations up and downstream.

The characteristic roots k_n are calculated by evaluating equation 3.13 at the boundary r=r_t subject to boundary condition 3.9. The values k_n just become the roots of:

$$J_1(k_n r_t) Y_1(k_n r_h) - J_1(k_n r_h) Y_1(k_n r_t) \tag{3.16}$$

The coefficients C_n are just a function of the hub and tip radius, defined explicitly as:

$$C_n = \frac{-2a(w r_t)}{(k_n r_t)^2} \begin{Bmatrix} r_t^2 \left[J_0(k_n r_t) Y_1(k_n r_h) - J_1(k_n r_h) Y_0(k_n r_t) \right] \\ - r_h^2 \left[J_0(k_n r_h) Y_1(k_n r_h) - J_1(k_n r_h) Y_0(k_n r_h) \right] \\ \hline r_t^2 \left[J_0(k_n r_t) Y_1(k_n r_h) - J_1(k_n r_h) Y_0(k_n r_t) \right]^2 \\ - r_h^2 \left[J_0(k_n r_h) Y_1(k_n r_h) - J_1(k_n r_h) Y_0(k_n r_h) \right]^2 \end{Bmatrix} \tag{3.17}$$

Marble (1964) also defines C_n in an integral form (Marble, 1964; Eq. 4-21) as:

$$C_n = \frac{a(wr_t)}{\left(k_n^{\,2} v_n r_t\right)} \int_{r_h}^{r_t} a^{\,2} \left[J_1(k_n a) Y_1(k_n r_h) - J_1(k_n r_h) Y_1(k_n a) \right] da \qquad (3.18)$$

Our investigation of his work has revealed that equation 3.18 should be corrected except for a typographical error [in Marble, 1964; Eq. 4-21)] on the r_t term in the denominator to become:

$$C_n = \frac{a(wr_t)}{\left(k_n^{\,2} v_n r_t^{\,2}\right)} \int_{r_h}^{r_t} a^{\,2} \left[J_1(k_n a) Y_1(k_n r_h) - J_1(k_n r_h) Y_1(k_n a) \right] da \qquad (3.18a)$$

Solutions to equations 3.13-3.15 were plotted and compared to Marble's published results in Figure 3.2. The most obvious discrepancy occurs between the plots of the axial velocity perturbation. The findings of the magnitude of the axial velocity perturbation in Work *et al* (2006b) are twice as large as Marble (1964). No specific cause has been identified at this time.

One interesting feature of equations 3.13-3.15 may provide some insight. A close examination of equations 3.13-3.15 shows complete independence between the velocity perturbation solutions ($u^{(1)}$ & $w^{(1)}$) and the base axial flow ($w^{(0)}$). The plots of the perturbation solutions remove dependence of the constants a and the blade wheel speed ω from the solution, but add a dependence on $w^{(0)}$. The base axial flow parameter used to generate the solutions by Work et al (2006b) is $w^{(0)}$=-0.5, which has little physical relevancy. This would require a base flow in the reverse direction through the machine. A second plot of the perturbation solutions is generated in Figure 3.3, which removes the $w^{(0)}$ dependence from the solution.

A significant finding is that although the perturbation solutions are now opposite in sign, the magnitude of the axial velocity is the same as Marble (1964). The radial

distribution is now about half the published magnitudes by Marble (1964). As a design aid, the flow perturbations in Figure 3.3 are significantly more useful, as there is no dependence on the base axial flow through the machine. Therefore, all subsequent plots will be plotted on a modified abscissa and benchmarked against Figure 3.3.

Actuator Disk Solutions, Marble (1964)

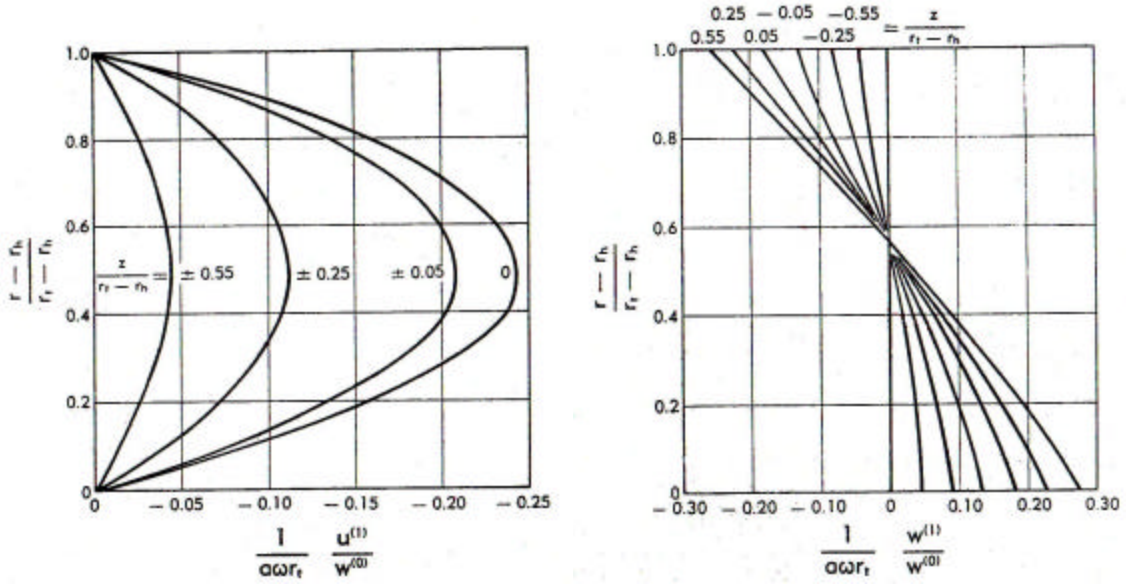

Actuator Disk Solutions, Work et al (2006)

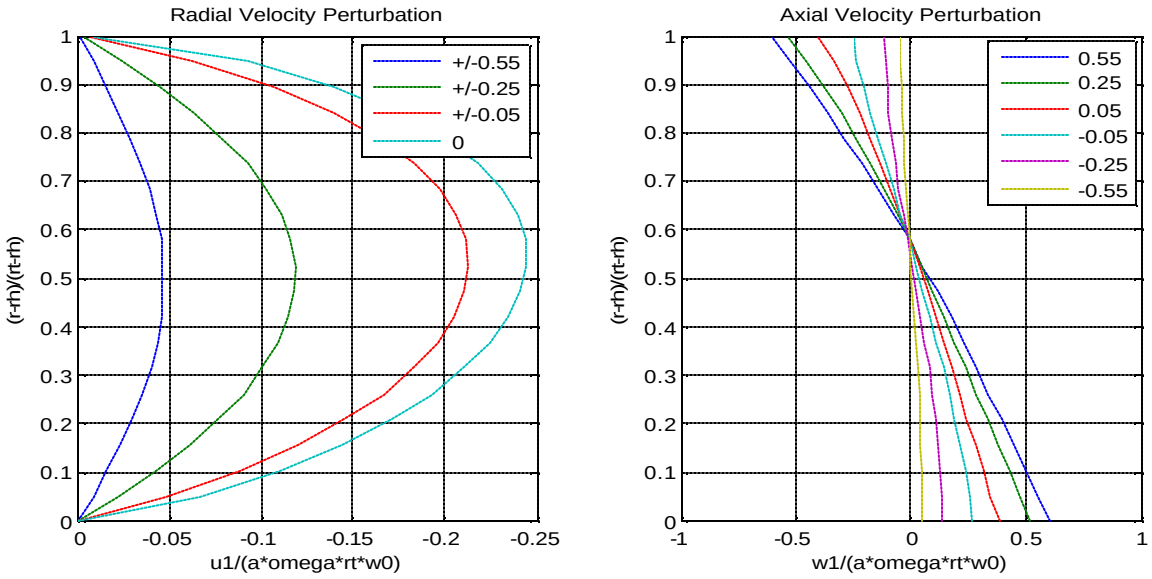

Figure 3.2

Actuator Disk Solutions, No $w^{(0)}$ Dependence

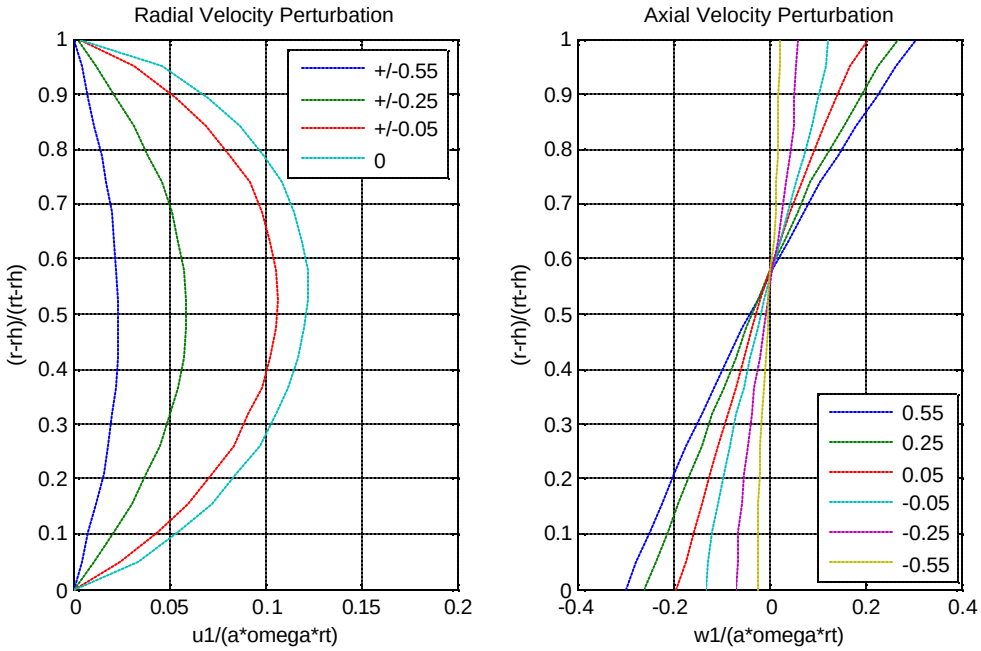

Figure 3.3

Asymptotic Actuator Disk Solutions

One of the central difficulties in developing perturbation solutions for the actuator disk problem lies in the evaluation of the Bessel functions. In 1964, this was primarily done either by hand or with tables, which could be a very time consuming process. As a result, Marble (1964) also developed an approximate solution based on an asymptotic evaluation of the Bessel functions. For sufficiently large hub to tip ratios ($\frac{r_h}{r_t} \geq 0.6$), the characteristic roots k_n may be approximated by:

$$k_n \approx \frac{np}{(r_t - r_h)} \tag{3.19}$$

Additionally, the Bessel functions which make up the basis of the perturbation solutions can also be approximated as

$$J_1(k_n r)Y_1(k_n r_h) - J_1(k_n r_h)Y_1(k_n r) \approx \frac{-2\left(r_t/r_h - 1\right)}{\sqrt{r/r_h}} \sin\left(\frac{np(r - r_h)}{(r_t - r_h)}\right) = 0 \tag{3.20}$$

$$J_0(k_n r)Y_1(k_n r_h) - J_1(k_n r_h)Y_0(k_n r) \approx \frac{-2\left(r_t/r_h - 1\right)}{\sqrt{r/r_h}} \cos\left(\frac{np(r - r_h)}{(r_t - r_h)}\right) = 0 \tag{3.21}$$

as defined in (Marble, 1964; Eq. 4-59, 4-50). However, a careful derivation of the asymptotic relationship reveals additional terms in the denominator outside of the trigonometric functions. Equations 3.20 and 3.21 should be replaced by:

$$J_1(k_n r)Y_1(k_n r_h) - J_1(k_n r_h)Y_1(k_n r) \approx \frac{-2\left(r_t/r_h - 1\right)}{np^2\sqrt{r/r_h}} \sin\left(\frac{np(r - r_h)}{(r_t - r_h)}\right) = 0 \tag{3.22}$$

$$J_0(k_n r)Y_1(k_n r_h) - J_1(k_n r_h)Y_0(k_n r) \approx \frac{-2\left(r_t/r_h - 1\right)}{np^2\sqrt{r/r_h}} \cos\left(\frac{np(r - r_h)}{(r_t - r_h)}\right) = 0 \tag{3.23}$$

The updated asymptotic relationships are plotted in Figure 3.4 for comparison with the Bessel Solutions shown in Figure 3.3. As can be seen, there is strong agreement.

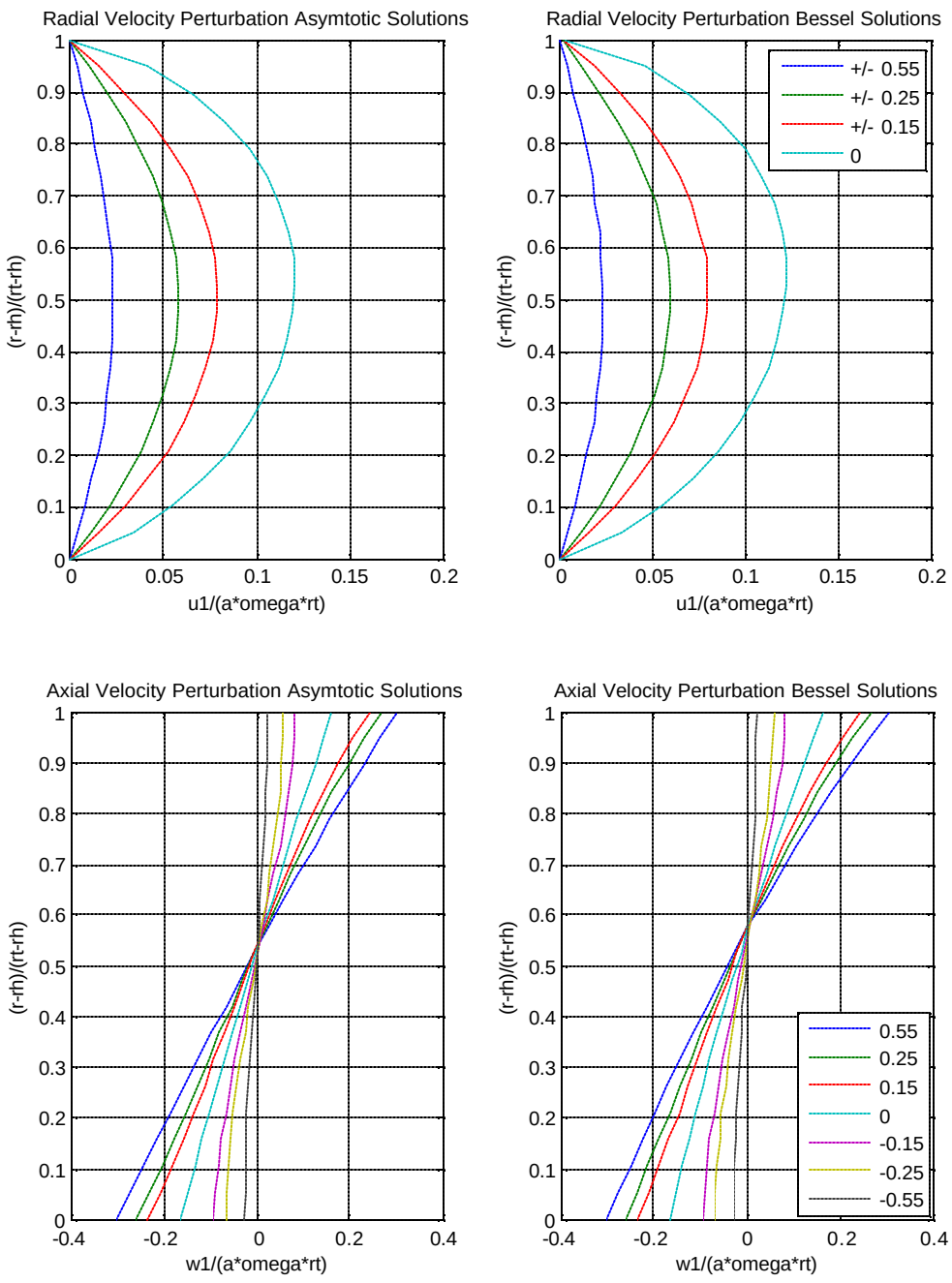
Radial Velocity Perturbation Asymtotic Solutions
(r-rh)/(rt-rh)
u1/(a*omega*rt)
Radial Velocity Perturbation Bessel Solutions
+/- 0.55
+/- 0.25
+/- 0.15
0
(r-rh)/(rt-rh)
u1/(a*omega*rt)
Axial Velocity Perturbation Asymtotic Solutions
(r-rh)/(rt-rh)
w1/(a*omega*rt)
Axial Velocity Perturbation Bessel Solutions
0.55
0.25
0.15
0
-0.15
-0.25
-0.55
(r-rh)/(rt-rh)
w1/(a*omega*rt)

Figure 3.4

Constant Hub Constant Tip Finite Chord Problem

A more complex, but physically more accurate analysis of the throughflow can be developed by considering a blade row with a finite chord length c. Governed by the same equations 3.6-3.9, the finite chord can be thought of as a summation of the effects of a series of actuator disks. The enthalpy jump for the finite chord is slightly modified to an asymmetric blade loading condition in which two thirds of the enthalpy increase is provided in the first half of the chord length. The enthalpy jump as a function of r (α) and z (β) becomes:

$$\frac{1}{w^{(0)}}\frac{\partial^2 h^{(1)}}{\partial a \partial b} = \frac{8}{3} a \frac{w}{c}\frac{a}{r_t} \qquad -\frac{c}{2} \le b \le 0 \tag{3.24}$$

$$\frac{1}{w^{(0)}}\frac{\partial^2 h^{(1)}}{\partial a \partial b} = \frac{8}{3} a \frac{w}{c}\frac{a}{r_t}\left(1-\frac{2z}{c}\right) \qquad 0 \le b \le \frac{c}{2} \tag{3.25}$$

Solutions for the finite chord [Marble, 1964; Eq. 4-23, 4-24, 4-27, & 4-28] are given as:

$$u^{(1)} = \int_{r_h}^{r_t}\int_{-c/2}^{c/2} \frac{1}{w^{(0)}}\frac{\partial^2 h^{(1)}}{\partial a \partial b} G(r,z;a,b)\,da\,db \tag{3.26}$$

$$\begin{aligned} w^{(1)} = &\int_{r_h}^{r_t}\int_{-\infty}^{z} \frac{1}{w^{(0)}}\frac{\partial^2 h^{(1)}}{\partial a \partial b} K(r,z;a,b)\,da\,db \\ &-\int_{r_h}^{r_t}\int_{z}^{\infty} \frac{1}{w^{(0)}}\frac{\partial^2 h^{(1)}}{\partial a \partial b} K(r,z;a,b)\,da\,db \\ &+2\int_{r_h}^{r_t}\int_{-\infty}^{z} \frac{1}{w^{(0)}}\frac{\partial^2 h^{(1)}}{\partial a \partial b} K(r,z;a,b)\,da\,db \end{aligned} \tag{3.27}$$

with:

$$G(r,z;a,b) = \sum_{1}^{\infty}\left\{ \frac{\begin{array}{c} a\left[J_1(k_n a)Y_1(k_n r_h) - J_1(k_n r_h)Y_1(k_n a)\right]* \\ \left[J_1(k_n r)Y_1(k_n r_h) - J_1(k_n r_h)Y_1(k_n r)\right] \end{array}}{k_n\left\{\begin{array}{l} r_t^{\,2}\left[J_0(k_n r_t)Y_1(k_n r_h) - J_1(k_n r_h)Y_0(k_n r_t)\right]^2 \\ -r_h^{\,2}\left[J_0(k_n r_h)Y_1(k_n r_h) - J_1(k_n r_h)Y_0(k_n r_h)\right]^2 \end{array}\right\}} e^{-k_n|z-b|}\right\} \tag{3.28}$$

$$K(r,z;a,b)=\sum_{1}^{\infty}\left\{\frac{\begin{array}{c}a\left[J_1(k_n a)Y_1(k_n r_h)-J_1(k_n r_h)Y_1(k_n a)\right]*\\ \left[J_0(k_n r)Y_1(k_n r_h)-J_1(k_n r_h)Y_0(k_n r)\right]\end{array}}{k_n\left\{\begin{array}{l}r_t{}^2\left[J_0(k_n r_t)Y_1(k_n r_h)-J_1(k_n r_h)Y_0(k_n r_t)\right]^2\\ -r_h{}^2\left[J_0(k_n r_h)Y_1(k_n r_h)-J_1(k_n r_h)Y_0(k_n r_h)\right]^2\end{array}\right\}}e^{-k_n|z-b|}\right\} \quad (3.29)$$

In the solution for the axial velocity (equation 3.27), Marble (1964) has multiple errors in his published equation. The first error is related to the limits of integration on the third term. The third term is the perturbation downstream, yet the integral is evaluated upstream. The second error also relates to the third term, and the Green's weighting function defined by $K(r,z;a,b)$. Because the Green's weighting function carries a "$e^{-k_n|z-b|}$" term, it must necessarily vanish far upstream and far downstream. However, the axial velocity perturbation far downstream should be twice that at the center of the chord, which can not be satisfied if the perturbation vanishes. The weighting function in the third term should not include the $e^{-k_n|z-b|}$ term. The final error involves the sign of the solution. When comparing equation 3.27 with 3.14 and 3.15, it is clear the two perturbation solutions are opposite in sign. When all of the above corrections are made, equations 3.27 and 3.29 become:

$$\begin{aligned}w^{(1)} = &-\int_{r_h}^{r_t}\int_{-\infty}^{z}\frac{1}{w^{(0)}}\frac{\partial^2 h^{(1)}}{\partial a\,\partial b}K_1(r,z;a,b)\,da\,db\\ &+\int_{r_h}^{r_t}\int_{z}^{\infty}\frac{1}{w^{(0)}}\frac{\partial^2 h^{(1)}}{\partial a\,\partial b}K_1(r,z;a,b)\,da\,db\\ &-2\int_{r_h}^{r_t}\int_{z}^{\infty}\frac{1}{w^{(0)}}\frac{\partial^2 h^{(1)}}{\partial a\,\partial b}K_2(r,z;a,b)\,da\,db\end{aligned} \quad (3.30)$$

with:

$$K_1(r,z;a,b)=\sum_1^{\infty}\left\{\frac{\begin{array}{c}a\left[J_1(k_n a)Y_1(k_n r_h)-J_1(k_n r_h)Y_1(k_n a)\right]*\\ \left[J_0(k_n r)Y_1(k_n r_h)-J_1(k_n r_h)Y_0(k_n r)\right]\end{array}}{k_n\left\{\begin{array}{l}r_t{}^2\left[J_0(k_n r_t)Y_1(k_n r_h)-J_1(k_n r_h)Y_0(k_n r_t)\right]^2\\ -r_h{}^2\left[J_0(k_n r_h)Y_1(k_n r_h)-J_1(k_n r_h)Y_0(k_n r_h)\right]^2\end{array}\right.}e^{-k_n|z-b|}\right\} \quad (3.31)$$

$$K_2(r,z;a,b)=\sum_1^{\infty}\left\{\frac{\begin{array}{c}a\left[J_1(k_n a)Y_1(k_n r_h)-J_1(k_n r_h)Y_1(k_n a)\right]*\\ \left[J_0(k_n r)Y_1(k_n r_h)-J_1(k_n r_h)Y_0(k_n r)\right]\end{array}}{k_n\left\{\begin{array}{l}r_t{}^2\left[J_0(k_n r_t)Y_1(k_n r_h)-J_1(k_n r_h)Y_0(k_n r_t)\right]^2\\ -r_h{}^2\left[J_0(k_n r_h)Y_1(k_n r_h)-J_1(k_n r_h)Y_0(k_n r_h)\right]^2\end{array}\right.}\right\} \quad (3.32)$$

A plot of the radial perturbation caused by the finite chord is reproduced in Figures 3.5ab. Both results by Marble (1964) and Work *et al* (2006b) are for the particular geometry defined by an aspect ratio ($\frac{r_t - r_h}{c}$) of 2.0. The Work *et al* (2006b) results are plotted without $w^{(0)}$ dependency (as discussed previously), which accounts for the difference in scale from Marble's work. It is important to note that the radial solution given by 3.26 was used to explicitly produce the perturbation results, however, a very fundamental discrepancy between the plotted results must be settled.

The error in question is the relationship between the upstream (negative axial position) and downstream (positive axial position) perturbation magnitudes. In Marble's (1964) work, the perturbation downstream is larger than that upstream. However, in Work *et al* (2006b), the opposite relationship is found. A careful analysis of an increasing finite chord beginning from an actuator disk provides some insight.

Recalling the enthalpy jump given by equations 3.24 and 3.25, it is noted that the total enthalpy jump across the chord length is equivalent to the enthalpy jump created by the actuator disk equation 3.8. As a result, when the chord length *c* approaches zero (aspect ratio $=\infty$), the finite chord solution converges on the actuator disk solution.

Figure 3.5c shows the finite chord radial perturbation is equivalent to the superimposed actuator disk result, shown in Figure 3.5c as plus symbols in comparison.

a

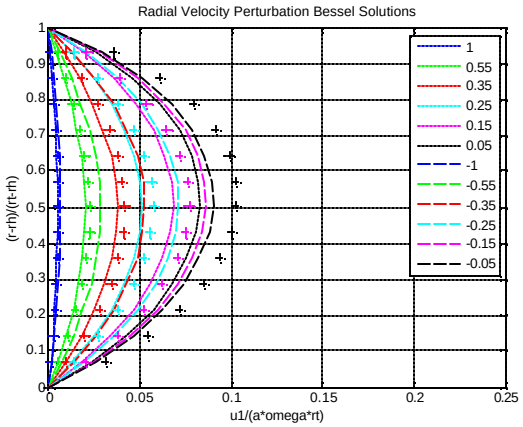

$$\frac{r_t - r_h}{c} = 2$$

b

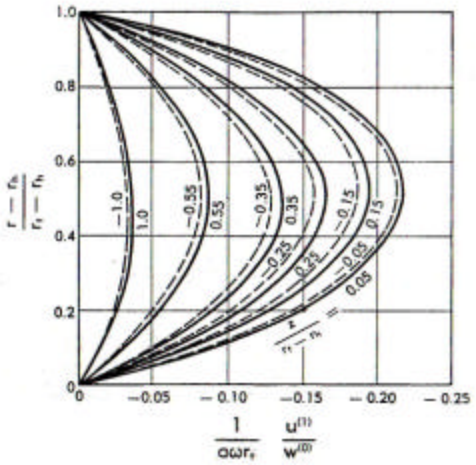

$$\frac{r_t - r_h}{c} = 2$$

c

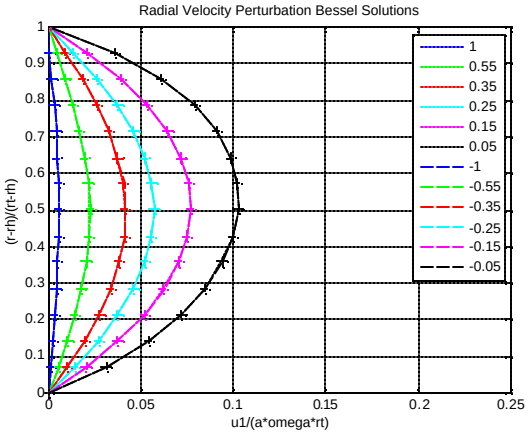

$$\frac{r_t - r_h}{c} \approx \infty$$

d

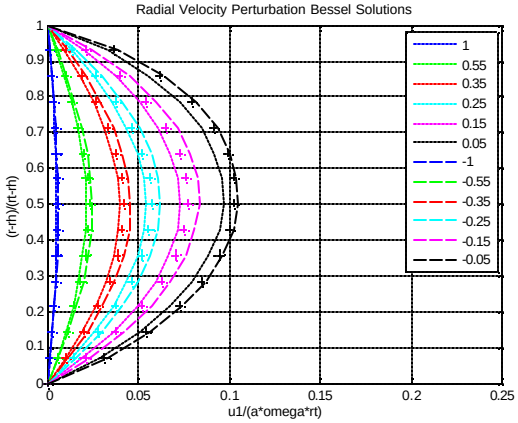

$$\frac{r_t - r_h}{c} = 5$$

Actuator disk (+) solution superimposed

Figure 3.5

As the actuator disk expands to a finite chord with an aspect ratio of five (Figure 3.5d), the separation from the upstream and downstream perturbation becomes apparent. The upstream perturbation is necessarily larger due to the type of asymmetry associated with the blade row. Because two-thirds of the enthalpy jump occurs on the leading (upstream) half of the finite chord, the center of the enthalpy jump no longer occurs at z=0, as was the case in the actuator disk problem. In fact, the center of the enthalpy jump now occurs at a point upstream ($z < 0$). Given a point outside of the finite chord, the finite chord can now be approximated as an actuator disk at the upstream center of the enthalpy jump. This center shift necessarily requires the perturbation at an upstream point to be larger than the corresponding downstream point because, in essence, the upstream point is closer to the source causing the perturbation. This reality is violated in Marble's (1964) finite chord radial perturbation distributions (Figure 3.5b).

When the finite chord is increased until the aspect ratio exactly matches the result produced in Marble (1964), a two additional inconsistencies are revealed. Clearly, the difference between the upstream and downstream radial perturbations is larger in the solutions generated by Work *et al* (2006b), although no specific cause has been identified at this time. Another point of interest is axial position $\frac{z}{r_t - r_h} = \pm 0.05$. While not entirely obvious, this position is inside the finite chord, near the midpoint. Because the radial perturbation is a function of distance from the source, the perturbation caused by the leading edge of the blade has already begun to dissipate before it reaches the trailing edge, as well as any other point inside the chord. As a result, the perturbation at $\frac{z}{r_t - r_h} = \pm 0.05$ caused by an actuator disk at z=0 is actually larger than the perturbation

created by a finite chord with a distributed source surrounding the point in question. The closer a point inside the chord lies towards the leading or trailing edge of the blade, the less likely the perturbation from the actuator disk will be larger than that of the finite chord. This phenomenon interestingly is not captured in the Marble (1964) result despite the use of the same solution function (equation 3.26).

The axial perturbation solutions are somewhat easier to compare because the effect of a finite chord is quite small for blade rows with an aspect ratio greater than one. The modified axial perturbation solution given by equation 3.30 is plotted along with the corresponding actuator disk results in Figure 3.6. With the noted exception of the magnitude and sign of the solution, which has been previously discussed for the actuator disk problem, the solutions are in good agreement, indicating the modifications to equation 3.27 are indeed correct.

Marble (1964)

Actuator Disk

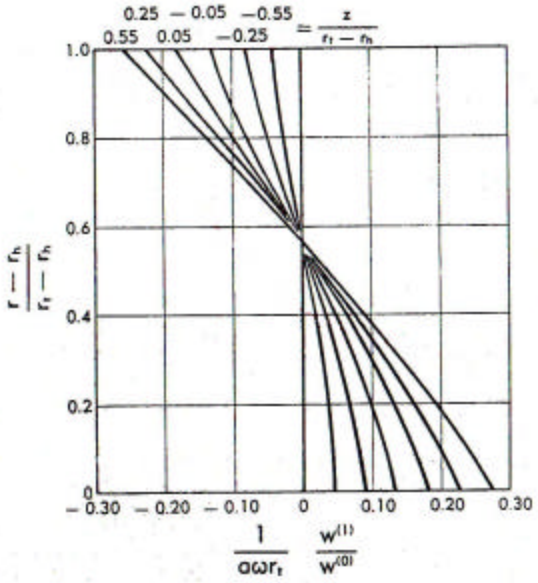

Finite Chord

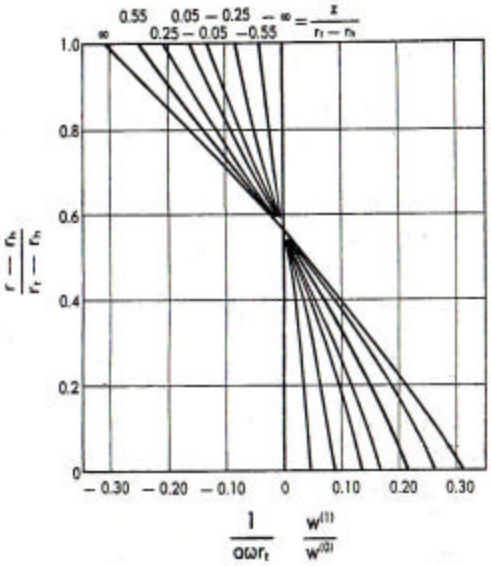

Work *et al* (2006b)

Actuator Disk

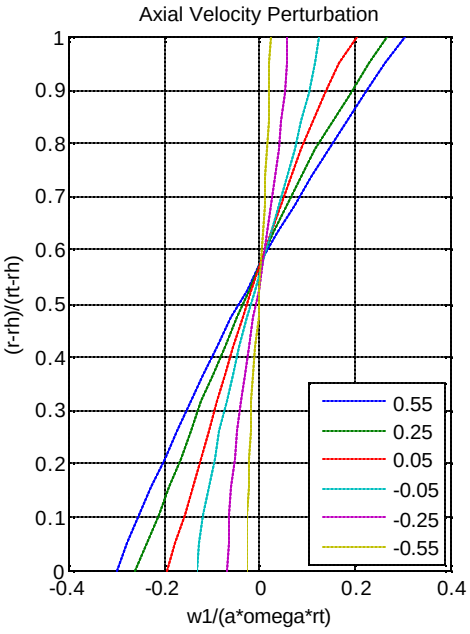

Finite Chord

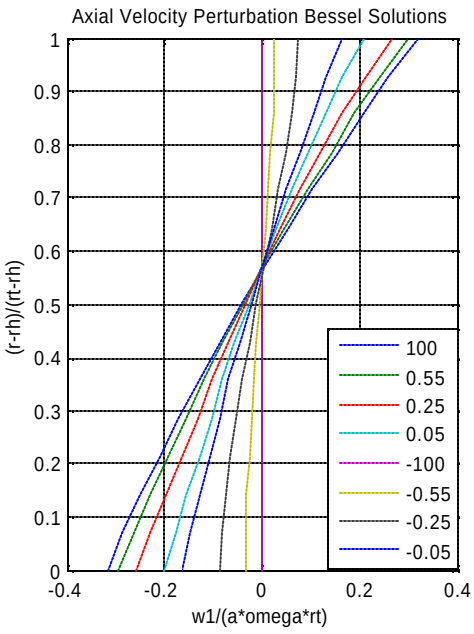

Figure 3.6

Variable Hub Constant Tip Problem

Up to this point in the present work, all sources of the radial and axial perturbations have been caused by a blade row. The variable hub problem is an investigation of a geometric source caused by a change in the cross sectional area (Figure 3.7).

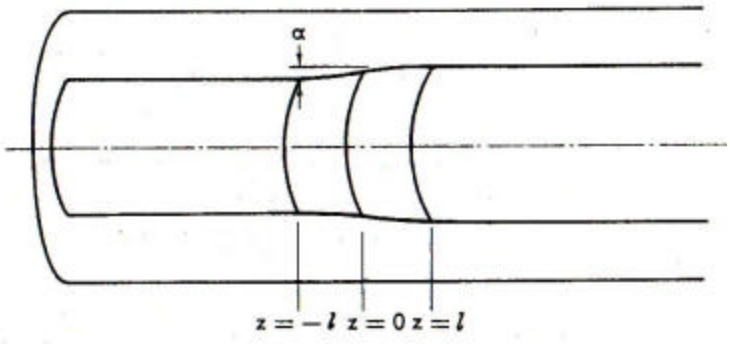

Figure 3.7

The perturbations are again governed by equations 3.6 and 3.7, subject to the boundary condition equation 3.10 and:

$$u^{(1)}(r_h, z) = w^{(0)} \frac{dr_h}{dz} \tag{3.33}$$

$$u^{(1)}(r_t, z) = 0 \tag{3.34}$$

Equation 3.33 defines the radial perturbation as the slope of the hub, which is then given by [Marble, 1964; Eq. 5-11]:

$$f_h(z) = \frac{pr_h}{2l} \cos\left(\frac{pz}{2l}\right) \qquad (|z| \geq l) \tag{3.35}$$

$$f_h(z) = 0 \qquad (|z| \geq l) \tag{3.36}$$

In order to generate the physical hub profile, equation 3.35 is integrated yielding:

$$F_h(z) = r_h \sin\left(\frac{pz}{2l}\right) + C \qquad (|z| \geq l) \tag{3.37}$$

There appears to be a significant limitation with the hub profile given by equation 3.37. Assuming a positive constant C, the hub slope will change by $2r_h$. In order to maintain a physically significant geometry, the hub to tip ratio ($\frac{r_h}{r_t}$) must be less than 0.5. Anything larger will create a change in the hub profile which is larger than the blade height. A more general hub profile can be constructed as:

$$F_h = a\sin\left(\frac{pz}{2l}\right) + C \qquad (|z| \le l) \tag{3.38}$$

Where $a = \frac{r_{h0}}{m}$, and r_{h0} is the hub radius at z=0, m is a scaling constant, and C= r_{h0}.

A specific example of a hub profile given by equation 3.38 is given in Figure 3.8.

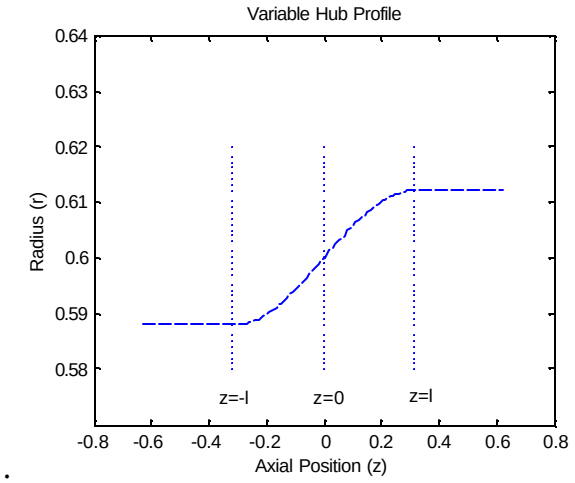

Figure 3.8

Given the new hub profile equation 3.38, the hub slope equation 3.35 now becomes:

$$f_h(z) = \frac{p\,a}{2l}\cos\left(\frac{pz}{2l}\right) \qquad (|z| \ge l) \tag{3.39}$$

This subtle change is significant because a Fourier transform of the boundary shape is taken in order to generate solutions to the radial and axial perturbation solutions.

All subsequent equations developed by Marble [(1964); Eq. 5-13 – 5.19, 5-21 – 5-23] must be modified to account for the new hub profile. Fortunately these changes only require a simple substitution of a in place of r_h in the terms outside of the Bessel functions. The solution for the radial perturbation given the new hub profile becomes:

$$\frac{u^{(1)}}{w^{(0)}} = -\frac{ap^2}{2l^2}\sum_1^\infty \frac{\cosh(k_n l)}{(p/2l)^2 + k_n^2}\left\{\begin{array}{l}\dfrac{[J_1(k_n r)Y_1(k_n r_t) - J_1(k_n r_t)Y_1(k_n r)]}{r_h[J_0(k_n r_h)Y_1(k_n r_t) - J_1(k_n r_t)Y_0(k_n r_h)]} \\ + r_t[J_1(k_n r_h)Y_0(k_n r_t) - J_0(k_n r_t)Y_1(k_n r_h)]\end{array}\right\} e^{-k_n|z|} \qquad (z > |l|) \tag{3.40}$$

$$\begin{aligned}\frac{u^{(1)}}{w^{(0)}} &= \frac{pa}{2l}\left[\frac{I_1\left(\frac{pr}{2l}\right)K_1\left(\frac{pr_t}{2l}\right) - I_1\left(\frac{pr_t}{2l}\right)K_1\left(\frac{pr}{2l}\right)}{I_1\left(\frac{pr_h}{2l}\right)K_1\left(\frac{pr_t}{2l}\right) - I_1\left(\frac{pr_t}{2l}\right)K_1\left(\frac{pr_h}{2l}\right)}\right]\cos\left(\frac{pz}{2l}\right) \\ &\quad -\frac{ap^2}{2l^2}\sum_1^\infty \frac{\cosh(k_n l)}{(p/2l)^2 + k_n^2}\left\{\begin{array}{l}\dfrac{[J_1(k_n r)Y_1(k_n r_t) - J_1(k_n r_t)Y_1(k_n r)]}{r_h[J_0(k_n r_h)Y_1(k_n r_t) - J_1(k_n r_t)Y_0(k_n r_h)]} \\ + r_t[J_1(k_n r_h)Y_0(k_n r_t) - J_0(k_n r_t)Y_1(k_n r_h)]\end{array}\right\} e^{-k_n|z|}\end{aligned} \qquad (z \le |l|) \tag{3.41}$$

where $I_1(x)$ and $K_1(x)$ are modified Bessel functions of the first and second kind, respectively.

The axial perturbation may be stated as:

$$\frac{w^{(1)}}{w^{(0)}} = \frac{ap^2}{2l^2}\sum_1^\infty \frac{\cosh(k_n l)}{(p/2l)^2 + k_n^2}\left\{\begin{array}{l}\dfrac{[J_0(k_n r)Y_1(k_n r_t) - J_1(k_n r_t)Y_0(k_n r)]}{r_h[J_0(k_n r_h)Y_1(k_n r_t) - J_1(k_n r_t)Y_0(k_n r_h)]} \\ + r_t[J_1(k_n r_h)Y_0(k_n r_t) - J_0(k_n r_t)Y_1(k_n r_h)]\end{array}\right\} e^{-k_n|z|} \quad (-\infty \le z \le -l) \tag{3.42}$$

$$\begin{aligned}\frac{w^{(1)}}{w^{(0)}} &= \frac{pa}{2l}\left[\frac{I_0\left(\frac{pr}{2l}\right)K_1\left(\frac{pr_t}{2l}\right) - I_1\left(\frac{pr_t}{2l}\right)K_0\left(\frac{pr}{2l}\right)}{I_1\left(\frac{pr_h}{2l}\right)K_1\left(\frac{pr_t}{2l}\right) - I_1\left(\frac{pr_t}{2l}\right)K_1\left(\frac{pr_h}{2l}\right)}\right]\left(1 + \sin\left(\frac{pz}{2l}\right)\right) \\ &\quad + \frac{ap^2}{2l^2}\sum_1^\infty \frac{1 + e^{-k_n l}\sinh(k_n z)}{(p/2l)^2 + k_n^2}\left\{\begin{array}{l}\dfrac{[J_0(k_n r)Y_1(k_n r_t) - J_1(k_n r_t)Y_0(k_n r)]}{r_h[J_0(k_n r_h)Y_1(k_n r_t) - J_1(k_n r_t)Y_0(k_n r_h)]} \\ + r_t[J_1(k_n r_h)Y_0(k_n r_t) - J_0(k_n r_t)Y_1(k_n r_h)]\end{array}\right\}\end{aligned} \qquad (-l \le z \le l) \tag{3.43}$$

$$\frac{w^{(1)}}{w^{(0)}} = \frac{pa}{l}\left[\frac{I_0\left(\frac{pr}{2l}\right)K_1\left(\frac{pr_t}{2l}\right) - I_1\left(\frac{pr_t}{2l}\right)K_0\left(\frac{pr}{2l}\right)}{I_1\left(\frac{pr_h}{2l}\right)K_1\left(\frac{pr_t}{2l}\right) - I_1\left(\frac{pr_t}{2l}\right)K_1\left(\frac{pr_h}{2l}\right)}\right] \qquad (3.44)$$

$$+\frac{ap^2}{2l^2}\sum_1^\infty \frac{2-e^{-k_n z}\cosh(k_n l)}{(p/2l)^2 + k_n{}^2}\left\{\begin{array}{l}\dfrac{\left[J_0(k_n r)Y_1(k_n r_t) - J_1(k_n r_t)Y_0(k_n r)\right]}{r_h\left[J_0(k_n r_h)Y_1(k_n r_t) - J_1(k_n r_t)Y_0(k_n r_h)\right]} \\ + r_t\left[J_1(k_n r_h)Y_0(k_n r_t) - J_0(k_n r_t)Y_1(k_n r_h)\right]\end{array}\right\} \qquad (l \le z)$$

The resulting solutions for the radial and axial perturbation are given in Figure 3.9. Because the solutions are given in terms of $w^{(0)}$, all plots will now contain a $\frac{1}{w^{(0)}}$ term along the abscissa. The radial velocity perturbation has the expected results that points along the hub have a perturbation equal to the slope of the hub. In general, all boundary conditions are satisfied. The resulting axial perturbation takes a shape upstream similar to that caused by a blade row. The perturbation at the hub is negative, while the perturbation at the tip is positive. As the hub begins to increase towards the tip, decreasing the cross sectional area, the perturbation becomes positive across the entire height of the blade. The axial perturbation increases most significantly along the hub boundary as expected. Far downstream, it is noted that the axial perturbation is again just twice that at z=0, which is a result of the continuity equation 3.7, and the radial perturbation symmetry.

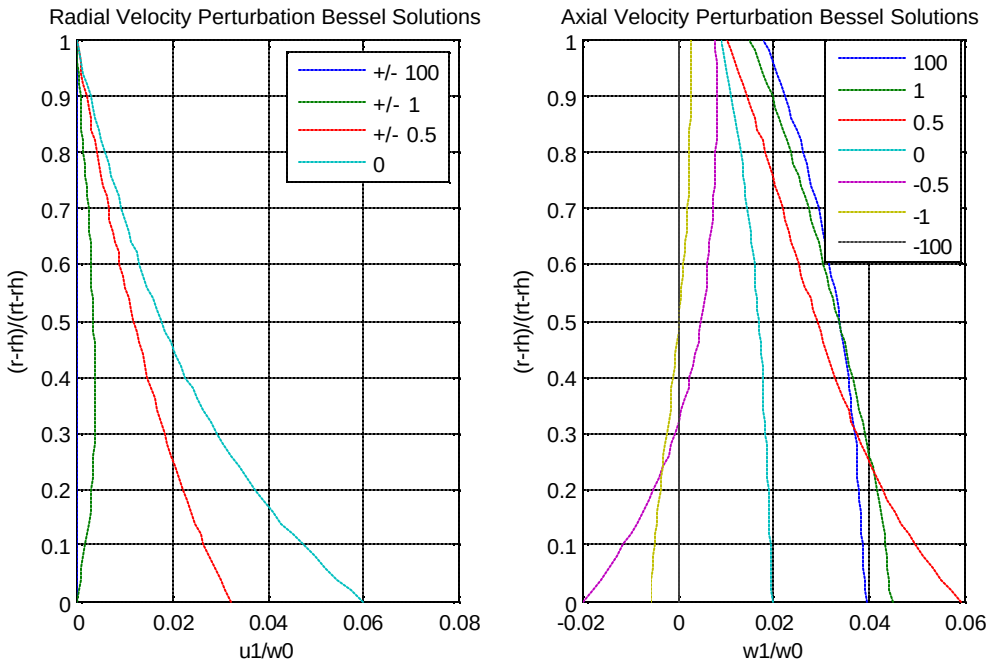

Figure 3.9

Variable Hub Constant Tip Asymptotic Solution

While no benchmark plots exist in Marble (1964) for the Bessel solutions to the variable hub geometry, an asymptotic solution to the axial perturbation [Marble, 1964; Eq 7-67 – 7-70] is provided as:

$$\frac{w^{(1)}(r,z)}{w^{(0)}} = a\left[\frac{1}{(r_t/r_h)^2-1}+\frac{1}{2}T(r)\right]\frac{1}{2}\cosh\left(p\frac{l}{r_t-r_h}\right)e^{p\frac{z}{r_t-r_h}} \qquad z\le -l \tag{3.45}$$

$$\frac{w^{(1)}(r,z)}{w^{(0)}} = a\left[\frac{1}{(r_t/r_h)^2-1}+\frac{1}{2}T(r)\right]\left(e^{-p\frac{l}{r_t-r_h}}\sinh\left(p\frac{z}{r_t-r_h}\right)-\sin\left(\frac{pz}{2l}\right)\right) \qquad -l\le z\le l \tag{3.46}$$
$$+\frac{a}{(r_t/r_h)^2-1}\left(1+\sin\left(\frac{pz}{2l}\right)\right)$$

$$\frac{w^{(1)}(r,z)}{w^{(0)}} = a\left[\frac{2}{(r_t/r_h)^2-1}+T(r)\right]\left(1-\frac{1}{2}\cosh\left(p\frac{l}{r_t-r_h}\right)e^{-p\frac{z}{r_t-r_h}}\right) \qquad l\le z \tag{3.47}$$
$$+\frac{2a}{(r_t/r_h)^2-1}$$

with:

$$T(r) = -\frac{pr_h}{l}\left[\frac{I_0\left(\frac{pr}{2l}\right)K_1\left(\frac{pr_t}{2l}\right) - I_1\left(\frac{pr_t}{2l}\right)K_0\left(\frac{pr}{2l}\right)}{I_1\left(\frac{pr_h}{2l}\right)K_1\left(\frac{pr_t}{2l}\right) - I_1\left(\frac{pr_t}{2l}\right)K_1\left(\frac{pr_h}{2l}\right)}\right] \tag{3.48}$$

A fundamental problem with the asymptotic solution is that the axial perturbation far downstream is not twice that at z=0. This can be shown by simply evaluating equation 3.46 at z=0 to reveal:

$$\frac{w^{(1)}(r,0)}{w^{(0)}} = a\left[\frac{1}{(r_t/r_h)^2 - 1} + \frac{1}{2}T(r)\right](0) + \frac{a}{(r_t/r_h)^2 - 1}(1) \quad -l \le z \le l \tag{3.49}$$

Whereas equation 3.47 evaluated at ∞ becomes:

$$\frac{w^{(1)}(r,\infty)}{w^{(0)}} = a\left[\frac{2}{(r_t/r_h)^2 - 1} + T(r)\right](1) + \frac{2a}{(r_t/r_h)^2 - 1} \qquad l \le z \tag{3.50}$$

A derivation of the asymptotic solutions might reveal the specific error in equation 3.47 or 3.48, but is outside the scope of this work. However, a plot of the asymptotic axial perturbation (Figure 3.10) reveals more information. It appears the problem may lie with equation 3.50, which governs the points far downstream. Conceptually, the axial perturbation downstream should be larger due to the constriction, but this is not captured in the asymptotic solution. When examining the accuracy of equation 3.45 and 3.46, the general shape of the solution is similar to the Bessel solution, although the magnitude is smaller. The difference in magnitude most likely arises from the modification of the hub slope function for the Bessel solution. Another potential source of error could come as a result of the additional $\frac{1}{np^2}$ in the asymptotic functions

(equation 3.22 and 3.23). Again, these controversies should be settled by a derivation of the asymptotic solutions (equations 3.45-3.47).

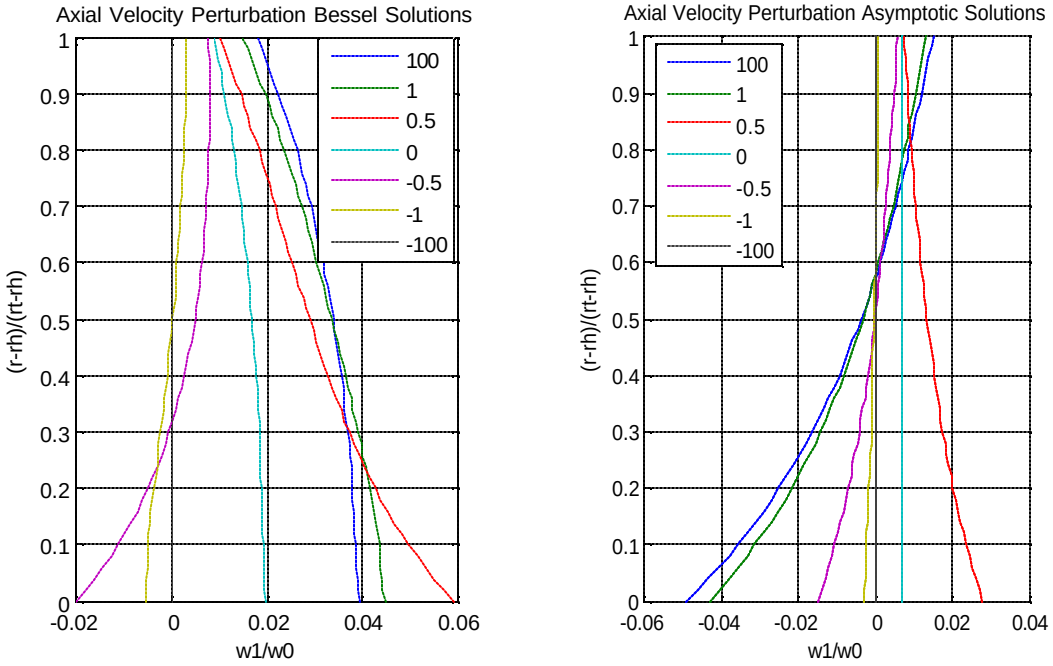

Figure 3.10

Variable Tip Constant Hub Problem

The axial and radial perturbations for the variable tip geometry are again governed by equations 3.6 and 3.7, subject to the boundary condition equation 3.10 and:

$$u^{(1)}(r_h, z) = 0 \tag{3.51}$$

$$u^{(1)}(r_t, z) = w^{(0)} \frac{dr_t}{dz} \tag{3.52}$$

where the tip slope is given by [Marble, 1964; Eq. 5-26]:

$$f_t(z) = \frac{pr_t}{2l} \cos\left(\frac{pz}{2l}\right) \qquad (|z| \geq l) \tag{3.53}$$

$$f_t(z) = 0 \qquad (|z| \geq l) \tag{3.54}$$

Equation 3.53 has a constraint in that it can not be used for a real gas turbine engine. The magnitude of the profile change from upstream to downstream, analogous to the variable hub problem, becomes $2r_t$. Only the case where the hub radius is zero, or does not exist, can this geometry be physically constructed. Furthermore, for this problem, the tip will diverge, increasing the cross sectional area. To be consistent with the variable hub problem, this section will treat the variable tip as a converging section (i.e., in the compressor). The modified tip slope then becomes:

$$f_t(z) = -\frac{p\,a}{2l}\cos\left(\frac{pz}{2l}\right) \qquad (|z| \geq l) \tag{3.56}$$

where $a = \frac{r_t}{m}$, and m is a scaling constant. A plot of varying tip of this class would take the form similar to Figure 3.11.

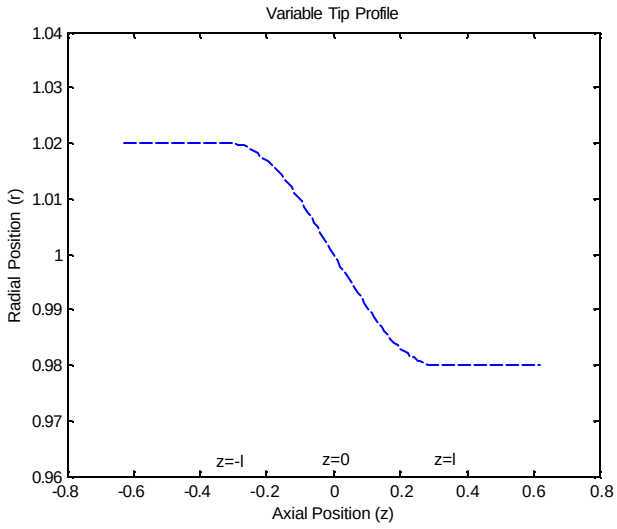

Figure 3.11

To generate the solutions for the variable tip problem, a simple substitution can be made into equations 3.40-3.44. Specifically, Marble [1964; Eq. 5-27, 5-28] outlines the procedure by substituting:

$$J_1(k_n r_h)Y_1(k_n r) - J_1(k_n r)Y_1(k_n r_h) \tag{3.57}$$

$$I_1\left(\frac{pr_h}{2l}\right)K_0\left(\frac{pr}{2l}\right) - I_0\left(\frac{pr}{2l}\right)K_1\left(\frac{pr_h}{2l}\right) \tag{3.58}$$

$$J_1(k_n r_h)Y_0(k_n r) - J_0(k_n r)Y_1(k_n r_h) \tag{3.59}$$

into equations 3.40-3.44 for:

$$J_1(k_n r)Y_1(k_n r_t) - J_1(k_n r_t)Y_1(k_n r) \tag{3.60}$$

$$I_1\left(\frac{pr}{2l}\right)K_0\left(\frac{pr_t}{2l}\right) - I_0\left(\frac{pr_t}{2l}\right)K_1\left(\frac{pr}{2l}\right) \tag{3.61}$$

$$J_0(k_n r)Y_1(k_n r_t) - J_1(k_n r_t)Y_0(k_n r) \tag{3.62}$$

If only the proceeding substitutions are made, the boundary constraints will not be satisfied. An additional substitution of:

$$I_1\left(\frac{pr_h}{2l}\right)K_1\left(\frac{pr}{2l}\right) - I_1\left(\frac{pr}{2l}\right)K_1\left(\frac{pr_h}{2l}\right) \tag{3.63}$$

must be made into equation 3.41 for:

$$I_1\left(\frac{pr}{2l}\right)K_1\left(\frac{pr_t}{2l}\right) - I_1\left(\frac{pr_t}{2l}\right)K_1\left(\frac{pr}{2l}\right) \tag{3.64}$$

These substitutions yield the following equations:

$$\frac{u^{(1)}}{w^{(0)}} = \frac{ap^2}{2l^2}\sum_1^\infty \frac{\cosh(k_n l)}{(p/2l)^2 + k_n^2}\left\{\begin{array}{l}\dfrac{[J_1(k_n r_h)Y_1(k_n r) - J_1(k_n r)Y_1(k_n r_h)]}{r_h[J_0(k_n r_h)Y_1(k_n r_t) - J_1(k_n r_t)Y_0(k_n r_h)]} \\ + r_t[J_1(k_n r_h)Y_0(k_n r_t) - J_0(k_n r_t)Y_1(k_n r_h)]\end{array}\right\} e^{-k_n|z|} \qquad (z > |l|) \tag{3.65}$$

$$\frac{u^{(1)}}{w^{(0)}} = -\frac{pa}{2l}\left[\frac{I_1\left(\frac{pr_h}{2l}\right)K_1\left(\frac{pr}{2l}\right) - I_1\left(\frac{pr}{2l}\right)K_1\left(\frac{pr_h}{2l}\right)}{I_1\left(\frac{pr_h}{2l}\right)K_1\left(\frac{pr_t}{2l}\right) - I_1\left(\frac{pr_t}{2l}\right)K_1\left(\frac{pr_h}{2l}\right)}\right]\cos\left(\frac{pz}{2l}\right)$$
$$\frac{ap^2}{2l^2}\sum_1^\infty \frac{\cosh(k_n l)}{(p/2l)^2 + k_n^2}\left\{\begin{array}{l}\dfrac{[J_1(k_n r_h)Y_1(k_n r) - J_1(k_n r)Y_1(k_n r_h)]}{r_h[J_0(k_n r_h)Y_1(k_n r_t) - J_1(k_n r_t)Y_0(k_n r_h)]} \\ + r_t[J_1(k_n r_h)Y_0(k_n r_t) - J_0(k_n r_t)Y_1(k_n r_h)]\end{array}\right\} e^{-k_n|z|} \qquad (z \le |l|) \tag{3.66}$$

$$\frac{w^{(1)}}{w^{(0)}} = -\frac{ap^2}{2l^2}\sum_1^\infty \frac{\cosh(k_n l)}{(p/2l)^2 + k_n^2}\left\{\begin{array}{l}\dfrac{[J_1(k_n r_h)Y_0(k_n r) - J_0(k_n r)Y_1(k_n r_h)]}{r_h[J_0(k_n r_h)Y_1(k_n r_t) - J_1(k_n r_t)Y_0(k_n r_h)]} \\ + r_t[J_1(k_n r_h)Y_0(k_n r_t) - J_0(k_n r_t)Y_1(k_n r_h)]\end{array}\right\} e^{-k_n|z|} \quad (-\infty \le z \le -l) \tag{3.67}$$

$$\frac{w^{(1)}}{w^{(0)}} = -\frac{pa}{2l}\left[\frac{I_1\left(\frac{pr_h}{2l}\right)K_0\left(\frac{pr}{2l}\right) - I_0\left(\frac{pr}{2l}\right)K_1\left(\frac{pr_h}{2l}\right)}{I_1\left(\frac{pr_h}{2l}\right)K_1\left(\frac{pr_t}{2l}\right) - I_1\left(\frac{pr_t}{2l}\right)K_1\left(\frac{pr_h}{2l}\right)}\right]\left(1+\sin\left(\frac{pz}{2l}\right)\right)$$
$$-\frac{ap^2}{2l^2}\sum_1^\infty \frac{1+e^{-k_n l}\sinh(k_n z)}{(p/2l)^2 + k_n^2}\left\{\begin{array}{l}\dfrac{[J_1(k_n r_h)Y_0(k_n r) - J_0(k_n r)Y_1(k_n r_h)]}{r_h[J_0(k_n r_h)Y_1(k_n r_t) - J_1(k_n r_t)Y_0(k_n r_h)]} \\ + r_t[J_1(k_n r_h)Y_0(k_n r_t) - J_0(k_n r_t)Y_1(k_n r_h)]\end{array}\right\} \quad (-l \le z \le l) \tag{3.68}$$

$$\frac{w^{(1)}}{w^{(0)}} = -\frac{pa}{l}\left[\frac{I_1\left(\frac{pr_h}{2l}\right)K_0\left(\frac{pr}{2l}\right) - I_0\left(\frac{pr}{2l}\right)K_1\left(\frac{pr_h}{2l}\right)}{I_1\left(\frac{pr_h}{2l}\right)K_1\left(\frac{pr_t}{2l}\right) - I_1\left(\frac{pr_t}{2l}\right)K_1\left(\frac{pr_h}{2l}\right)}\right]$$
$$-\frac{ap^2}{2l^2}\sum_1^\infty \frac{2-e^{-k_n z}\cosh(k_n l)}{(p/2l)^2 + k_n^2}\left\{\begin{array}{l}\dfrac{[J_1(k_n r_h)Y_0(k_n r) - J_0(k_n r)Y_1(k_n r_h)]}{r_h[J_0(k_n r_h)Y_1(k_n r_t) - J_1(k_n r_t)Y_0(k_n r_h)]} \\ + r_t[J_1(k_n r_h)Y_0(k_n r_t) - J_0(k_n r_t)Y_1(k_n r_h)]\end{array}\right\} \quad (l \le z) \tag{3.69}$$

Given these modifications, the radial and axial velocity perturbations are determined (Figure 3.12). The radial velocity perturbation appears exactly as expected. The variable tip perturbations are larger than that of the previous variable hub problem, because the constriction is larger. This is a direct result of the definition of a in each problem. The radial perturbation is negative due to the negative slope of the tip profile.

The axial velocity perturbation is clearly incorrect. At the tip along the converging section, the velocity perturbation should be positive. Furthermore, upstream from the geometry change, a similar perturbation would be expected from either the variable hub or variable tip, yet the perturbations are opposite. In fact, the entire solution appears to be mirrored.

When the hub slope was modified to create a diverging section, a negative sign was carried through the perturbation formulas. This had the appropriate effect on the radial solution (negative perturbation caused by a negative slope), but it also negated the axial velocity perturbation. Even if the solution was constructed as a diverging section as originally prescribed by equation 3.53, the axial solution would still be incorrect. By removing the negative sign, axial velocity would now be increasing for a diverging section, which is also not true. However, if a negative sign is divided out of equations 3.67-3.69, the resulting plot much more closely resembles what should physically occur (Figure 3.13). Although a specific cause of the mirrored axial velocity perturbation has not been identified at this time, it is believed a negative sign should be taken of the axial perturbation equations.

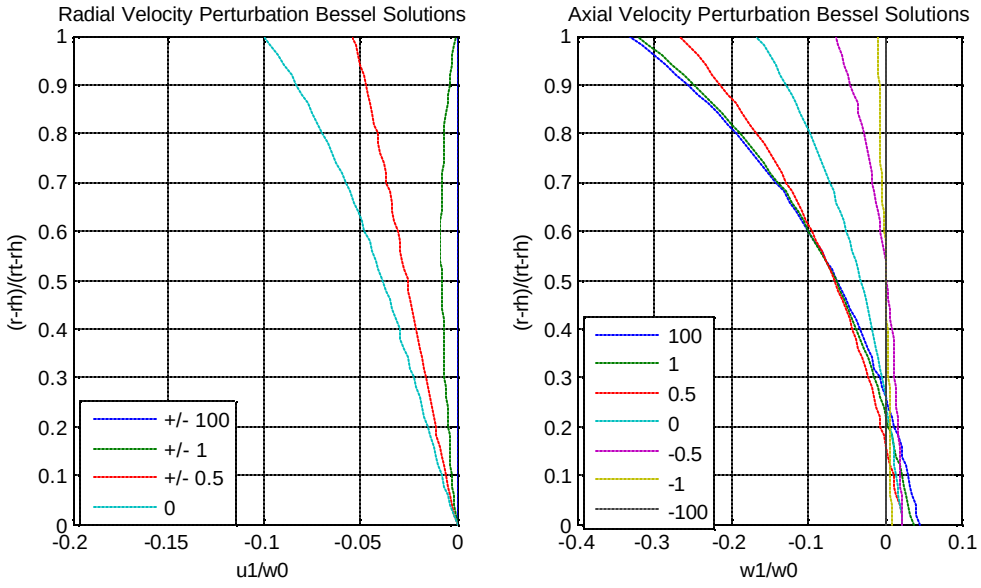

Figure 3.12

Modified Axial Perturbation

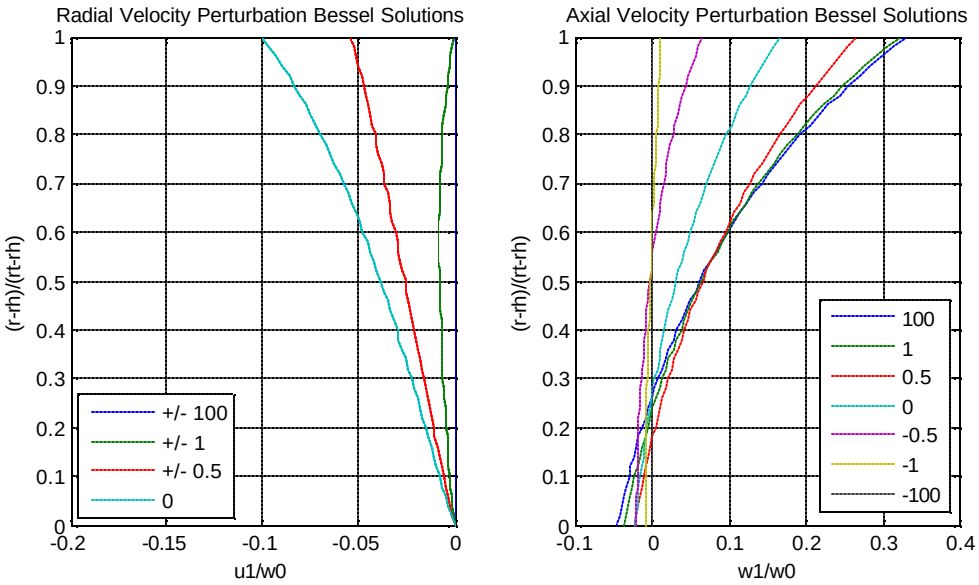

Figure 3.13

4. SUMMARY

In this work, the Reduced Order Meshless methodology was implemented on a series of one- and two-dimensional advection-diffusion problems, and two- and three-dimensional convection-diffusion problems. The linear advection diffusion problems show a significant improvement over other emerging meshless techniques in the ability to capture the boundary layer effects of high Peclet flows. At low Reynolds number flows, solutions have also been achieved. Current work is under way to expand the scope of work to include the nonlinear convection-diffusion problems of high Reynolds number. One of the major advantages of ROM is that no upwinding is needed to stabilize the results.

A second principle finding of this work was uncovered in the search to find an approximate three-dimensional Navier-Stokes solution, specifically related to the throughflow of a gas turbine engine. The seminal work of Marble (1964) on this topic was revisited and a number of inconsistencies were discovered. The most significant findings include actuator disk and finite chord solutions which are opposite in sign from the published Marble (1964) results. Additionally, radial perturbations are half as large as published for a given axial perturbation. Other errors include a missing factor on the asymptotic analysis of the actuator disk solution, and hub and tip slope functions which are severely restricted for the design of real gas turbine engines with a variable hub or tip. Furthermore, expressions to convert the variable hub problem to variable tip geometry are incomplete, and the asymptotic axial perturbation of a variable tip problem does not satisfy a key constraint of the continuity equation. This research will also be extended to definitively answer the questions raised in this work.

5. REFERENCES

Atluri, S.N., and Shengping, S., (2002), The Meshless Local Petrov-Galerkin (MLPG) Method, *Tech Science Press.*

Belytcshko, T., Lu, Y. Y., and Gu, L. (1994), Element-Free Galerkin Methods. *Int. J. Num. Meth. Eng.*, vol. 37, pp. 229–256.

Duarte, C. A., and Oden, J. T. (1996), An H-P Adaptive Method Using Clouds. *Comput.Methods Appl. Mech. Engrg.*, vol. 139, pp. 237–262.

Fang, C., McGee, O.G., and El-Aini, Y., (2005), "A Reduced-Order Meshless Energy Model for the Three-Dimensional Elastodynamics of Bladed Disk, Part II: Finite Element Benchmark Comparisons," *submitted for publication to the ASME Journal of Engineering for Gas Turbines and Power.;*

Lin,H., and Atluri, S. N. (2000), Meshless Local Petrov-Galerkin (MLPG) Method for Convection-Diffusion Problems. *Computer Modeling in Engineering & Sciences*, vol. 1 (2), pp. 45–60.

Liu, G.R., (2003), Mesh Free Methods – Moving Beyond the Finite Element Method, CRC Press.

Liu, W. K., Jun, S., and Zhang, Y. (1995), Reproducing Kernel Particle Methods. *Int. J. Num. Meth. Fluids*, vol. 20, pp. 1081–1106.

Lucy (1977), A Numerical Approach to the Testing of the Fission Hypothesis. *The Astro. J.*, vol. 8, pp. 1013–1024.

Marble, F.E. , (1964), "Three-Dimensional Flow in Turbomachines," in Aerodynamics of Turbines and Compressors, Volume X, W.R. Hawthorne (Editor), *High Speed Aerodynamics and Jet Propulsion*.

McGee, O.G., Fang, C., and El-Aini, Y., (2005), "A Reduced-Order Meshless Energy Model for the Three-Dimensional Elastodynamics of Bladed Disk, Part I: Theoretical Foundations," *submitted for publication to the ASME Journal of Engineering for Gas Turbines and Power.;*

McGee, O.G., Fang, C., (2005), "A Reduced-Order Integrated Design Synthesis for the Three-Dimensional Tailored Vibration Response and Flutter Control of High-Bypass Shroudless Fans," *submitted for publication to the ASME Journal of Engineering for Gas Turbines and Power.;*

McGee, O.G., Fang, C., and Work, D., 2006, "Existence and Smoothness of Three-Dimensional Navier-Stokes Transport Phenomena, Part I: Theory and Metrics," *to be submitted for publication to the ASME Journal of Fluids Engineering.*

Naroles, B., Touzot, G., and Villon, P. (1992), Generalizing the Finite Element Method: Diffuse Approximation and Diffuse Elements. *Comput.Mech.*, vol. 10, pp. 307–318.

Oñate, E., Idelsohn, S., Zienkiewicz, O. C., and Taylor, R. L. (1996), A Finite Point Method in Computational Mechanics. Application to Convective Transport and Fluid Flow. *Int. J. Num. Meth. Eng.*, vol. 39, pp. 3839–3866.

Shin, Y.S., and Chisum, J.E., (1997), "Modeling and Simulation of Underwater Shock Problems Using a Coupled Lagrangian-Eulerian Analysis Approach," *Shock and Vibration Digest, Vol. 4, p. 1-10.*

Work, D., Fang, C., and McGee, O.G., (2006a), "Existence and Smoothness of Three-Dimensional Navier-Stokes Transport Phenomena, Part II: Exact and Finite Volume Benchmark Comparisons," *to be submitted for publication to the ASME Journal of Fluids Engineering.*

Work, D. and McGee, O.G., (2006b), "Revisiting Marble's Three-Dimensional Flow in Turbomachines," *AIAA Journal*, to be published.

Zhu, T., Zhang, J. D., and Atluri, S. N. (1998a), A Local Boundary Integral Equation (LBIE) Method in Computational Mechanics, and a Meshless Discretization Approach. *Comput. Mech.*, vol. 21, pp. 223–235.

Zhu, T., Zhang, J. D.,and Atluri, S. N. (1998b): A Meshless Local Boundary Integral Equation (LBIE) Method for Solving Nonlinear Problems. *Comput.Mech.*, vol. 22, pp. 174–186.

6. APPENDIX A - ADDITIONAL TYPOGRAPHICAL ERRORS

1. [Marble 1964; Eq 5-23] is given as:

$$\frac{w^{(1)}}{w^{(0)}} = \frac{pa}{l}\left[\frac{I_0\left(\frac{pr}{2l}\right)K_1\left(\frac{pr_t}{2l}\right) - I_1\left(\frac{pr_t}{2l}\right)K_0\left(\frac{pr}{2l}\right)}{I_1\left(\frac{pr_h}{2l}\right)K_1\left(\frac{pr_t}{2l}\right) - I_1\left(\frac{pr_t}{2l}\right)K_1\left(\frac{pr}{2l}\right)}\right] \qquad (l \le z)$$
$$+ \frac{ap^2}{2l^2}\sum_1^\infty \frac{2 - e^{-k_n z}\cosh(k_n l)}{(p/2l)^2 + k_n^2}\left\{\begin{array}{l}\dfrac{[J_0(k_n r)Y_1(k_n r_t) - J_1(k_n r_t)Y_0(k_n r)]}{r_h[J_0(k_n r_h)Y_1(k_n r_t) - J_1(k_n r_t)Y_0(k_n r_h)]} \\ + r_t[J_1(k_n r_h)Y_0(k_n r_t) - J_0(k_n r_t)Y_1(k_n r_h)]\end{array}\right\}$$

The r in the modified Bessel function of the second kind should be corrected in the denominator of the first term to r_h:

$$\frac{w^{(1)}}{w^{(0)}} = \frac{pa}{l}\left[\frac{I_0\left(\frac{pr}{2l}\right)K_1\left(\frac{pr_t}{2l}\right) - I_1\left(\frac{pr_t}{2l}\right)K_0\left(\frac{pr}{2l}\right)}{I_1\left(\frac{pr_h}{2l}\right)K_1\left(\frac{pr_t}{2l}\right) - I_1\left(\frac{pr_t}{2l}\right)K_1\left(\frac{pr_h}{2l}\right)}\right] \qquad (l \le z) \qquad (3.44)$$
$$+ \frac{ap^2}{2l^2}\sum_1^\infty \frac{2 - e^{-k_n z}\cosh(k_n l)}{(p/2l)^2 + k_n^2}\left\{\begin{array}{l}\dfrac{[J_0(k_n r)Y_1(k_n r_t) - J_1(k_n r_t)Y_0(k_n r)]}{r_h[J_0(k_n r_h)Y_1(k_n r_t) - J_1(k_n r_t)Y_0(k_n r_h)]} \\ + r_t[J_1(k_n r_h)Y_0(k_n r_t) - J_0(k_n r_t)Y_1(k_n r_h)]\end{array}\right\}$$

2. [Marble 1964; Eq 7-65] is given as:

$$\frac{2r_h^2}{r_t^2 - r_h^2} = \frac{pr_h}{l}\left[\frac{I_0\left(\frac{pr}{2l}\right)K_1\left(\frac{pr_t}{2l}\right) - I_1\left(\frac{pr_t}{2l}\right)K_0\left(\frac{pr}{2l}\right)}{I_1\left(\frac{pr_h}{2l}\right)K_1\left(\frac{pr_t}{2l}\right) - I_1\left(\frac{pr_t}{2l}\right)K_1\left(\frac{pr_h}{2l}\right)}\right] \qquad (l \le z)$$
$$+ \frac{r_h p^2}{2l^2}\sum_1^\infty \frac{2 - e^{-k_n z}\cosh(k_n x)}{(p/2l)^2 + k_n^2}\left\{\begin{array}{l}\dfrac{[J_0(k_n r)Y_1(k_n r_t) - J_1(k_n r_t)Y_0(k_n r)]}{r_h[J_0(k_n r_h)Y_1(k_n r_t) - J_1(k_n r_t)Y_0(k_n r_h)]} \\ - r_t[J_1(k_n r_h)Y_0(k_n r_t) - J_0(k_n r_t)Y_1(k_n r_h)]\end{array}\right\}$$

The x should be replaced by l, the two bracketed terms in the denominator of the second term should be added together, instead of subtracted, to become:

$$\frac{2r_h^2}{r_t^2 - r_h^2} = \frac{pr_h}{l}\left[\frac{I_0\left(\frac{pr}{2l}\right)K_1\left(\frac{pr_t}{2l}\right) - I_1\left(\frac{pr_t}{2l}\right)K_0\left(\frac{pr}{2l}\right)}{I_1\left(\frac{pr_h}{2l}\right)K_1\left(\frac{pr_t}{2l}\right) - I_1\left(\frac{pr_t}{2l}\right)K_1\left(\frac{pr_h}{2l}\right)}\right]$$

$$+\frac{r_h p^2}{2l^2}\sum_1^\infty \frac{2 - e^{-k_n z}\cosh(k_n l)}{(p/2l)^2 + k_n^2}\left\{\frac{[J_0(k_n r)Y_1(k_n r_t) - J_1(k_n r_t)Y_0(k_n r)]}{r_h[J_0(k_n r_h)Y_1(k_n r_t) - J_1(k_n r_t)Y_0(k_n r_h)] + r_t[J_1(k_n r_h)Y_0(k_n r_t) - J_0(k_n r_t)Y_1(k_n r_h)]}\right\} \qquad (l \le z)$$

3. [Marble 1964; Eq 7-68] is given as:

$$\frac{w^{(1)}(r,z)}{w^{(0)}} = a\left[\frac{1}{(r/r_h)^2 - 1} + \frac{1}{2}T(r)\right]\frac{1}{2}\cosh\left(p\,\frac{l}{r_t - r_h}\right)e^{p\frac{z}{r_t - r_h}} \qquad z \le l$$

The domain should be corrected to:

$$\frac{w^{(1)}(r,z)}{w^{(0)}} = a\left[\frac{1}{(r/r_h)^2 - 1} + \frac{1}{2}T(r)\right]\frac{1}{2}\cosh\left(p\,\frac{l}{r_t - r_h}\right)e^{p\frac{z}{r_t - r_h}} \qquad z \le -l \qquad (3.45)$$